SAR Imaging in Frequency Scan Mode: System Optimization and Potentials for Data Volume Reduction

Nicola Gollin, Rolf Scheiber, Michele Martone, Paola Rizzoli, and Gerhard Krieger

***Abstract*—Frequency Scanning (FScan) is an innovative acquisition mode for Synthetic Aperture Radar (SAR) systems. The method is based on the frequency-dependent beam pointing capabilities of phased array antennas, artificially increased via the combined use of true time delays and phase shifters within the array antenna. By this, typical limitations of conventional SAR systems in terms of achievable swath width and azimuth resolution can be mitigated, and so a wide swath can be imaged maintaining a fine azimuthal resolution. In the first part of the paper we introduce the theoretical concept, which is necessary to evaluate the reduced echo window length with respect to equivalent stripmap data and the implications for the transmit pulse characterisation. An FScan sensor flying in a TerraSAR-X-like orbit is shown to be capable of imaging an 80 km wide swath with 1 m azimuth resolution. The resulting time-frequency properties of the recorded raw data make traditional SAR data compression algorithms like block-adaptive quantization (BAQ) highly inefficient in this case. Therefore, the second part of the paper investigates dedicated quantization methods for efficient data volume reduction in FScan systems. Different solutions are investigated and evaluated through simulations. Various transformations of the raw data have been exploited in order to optimize the encoding process, including deramping, Fast Fourier Transform (FFT) and blockwise approaches. Compared to standard BAQ in time domain, the suggested data compression methods significantly improve the resulting signal-to-quantization noise ratio, allowing for the reduction of the overall data volume by about 60% for the considered system scenario, while maintaining robustness in presence of inhomogeneous scene characteristics at the cost of a modest complexity increase for its on-board implementation.**

***Index Terms*—SAR, high-resolution wide-swath (HRWS), Frequency Scan (FScan), data volume reduction, quantization.**

I. INTRODUCTION

SYNTHETIC Aperture Radar (SAR) represents a well-recognized technique for remote sensing applications in present days, having been employed in a large number of spaceborne missions for more than forty years in a wide range of scientific and commercial applications (e.g. [1]–[4]). With conventional SAR, the mapping of a wider swath on ground can only be achieved by lowering the azimuth resolution, as done, e.g., with ScanSAR and TOPSAR modes [5], [6], which are able to acquire swath widths up to several hundreds of kilometers at a cost of reduced azimuth resolution of 10 m to 40 m. Differently, future SAR systems are oriented towards finer resolutions and larger swath widths. Recently developed high-resolution wide-swath (HRWS) architectures [7] are designed to mitigate this limitation by implementing new operation concepts such as SCan On REceive (SCORE) [8] in combination with multiple azimuth phase centers (MAPS) [9]. In addition, the echoes of several beams may be received in parallel, covering a wider swath in an effective way without the need for multiple bursts [10]. In this case, the blind ranges corresponding to transmit pulse events can be mitigated by selecting a variable pulse repetition interval (PRI) setting, as done, e.g., in staggered SAR [11] or slow PRI variation modes [12]. The imaging capabilities of future SAR sensors will also include very-high spatial resolution down to 1 m or below. A large transmit bandwidth can alternatively be used to map wider swaths. An example is given by the multi-frequency sub-pulse (MFSP) mode proposed in [10], [13], [14], according to which sub-pulses within the same PRI are used, occupying disjoint range frequency bands to simultaneously acquire multiple sub-swaths. In contrast, in the FScan mode, as proposed in [15] and also investigated in [16], a wide swath is illuminated by antenna patterns with continuously increasing or decreasing center frequency. Here, the chirp modulation can be selected in a favourable way to allow for a drastic reduction of the echo window length, at the expense of potentially large chirp durations. Differently from other wide-swath acquisition modes, such as ScanSAR, scalloping is not present in FScan data and larger duty cycles may also be operated. Moreover, the continuous acquisition does not degrade the azimuth resolution.

Such high-resolution systems generate a continuously increasing amount of raw data, posing new challenges in terms of on-board memory and downlink capacity. In this context, quantization of SAR raw data plays an essential role, as it defines the quality of the resulting SAR products as well as the required volume of data to be managed by the system.

For state-of-the-art SAR systems, Block-Adaptive Quantization (BAQ) represents a standard approach, by ensuring a feasible trade-off between achievable data compression and signal quality representation [17], [18]. Starting from BAQ, other techniques have been derived in the last years, such that the quantization scheme for a specific acquisition mode is usually optimized for the specific scenario in order to minimize the required data volume. Some examples of encoding optimization depending on the system characteristics include the Flexible Dynamic Block Adaptive Quantization (FDBAQ) scheme [19], [20] (utilized for the Sentinel-1 SAR mission),

The authors are with the Microwaves and Radar Institute, German Aerospace Center (DLR), 82234 Wessling, Germany. e-mail: Nicola.Gollin@dlr.de

and dedicated quantization concepts for multi-azimuth channel architectures [21] or staggered SAR systems [22].

The present paper aims at investigating system design aspects and possibilities for data volume reduction in the context of the FScan acquisition mode. The idea behind this technique is to illuminate a wider swath by a proper "sweeping" of the center frequency of the radar pulses by means of a frequency dependent (dispersive) beam pointing. Thus, the targeted area is illuminated with variable frequency along the range domain. This allows one to properly discriminate a range location not only in time (as in a conventional SAR system) but also in frequency. If a large enough chirp length is used, the echoes from the whole swath can be superimposed in time (i.e., they are received by the sensor in a shorter time interval) but they are still separable in the frequency domain. By means of a specific system parameters optimization, it is possible to show that the echo window length for such a system can be drastically reduced while still being able to acquire a wide swath in range and separate all the imaged targets.

The concept of FScan and the typical trade-offs for the system design and parameters are described in Section II, where a representative SAR system configuration is investigated as well. The peculiarity of such a system lies in the spectral characteristics of the acquired raw data. This leads to further considerations on the possibility to develop effective data volume reduction approaches for SAR systems operating in FScan mode. The description of the proposed methods is provided in Section III, where different solutions to efficiently encode the acquired FScan raw data are introduced. The proposed concepts are then analyzed in detail in Section IV, and a detailed performance assessment is carried out by simulations of synthetic SAR scenes. Finally, the paper is concluded in Section V, where an outlook on future research work is presented.

II. FSCAN MODE - ACQUISITION PRINCIPLE

The concept of the FScan acquisition mode has been initially introduced in [15] and further elaborated in [23]. The imaging principle consists of illuminating the desired swath with a variable center frequency. In other words, the center frequency f_0 of the transmitted wave impinging on ground varies with respect to the range position between $f_0 - \frac{B_{\mathrm{TX}}}{2}$ and $f_0 + \frac{B_{\mathrm{TX}}}{2}$, where B_{TX} is the transmitted bandwidth. This is made possible thanks to a specific hardware design in the antenna module, which includes both phase shifters and true time delay lines (TTDL), as described in [15]. Therefore, details on the hardware implementation are not further recalled in this paper.

A graphical representation of the FScan acquisition principle is presented in Figure 1. According to it, the radar echoes from the target area are not only separated in range time but also in range frequency: this means that the echoes from different targets on ground are mutually displaced in both the time domain, because of different pulse travelling times, and the frequency domain, as the impinging wave has a different center frequency depending on the range position itself. By comparing this approach with a conventional SAR (e.g. stripmap) system, a wider swath could be captured by means of a shorter echo window length (EWL) by illuminating first far-, then mid- and finally near-range, as also proposed for the concept of intrapulse beamsteering in [24]. If a sufficiently long chirp length τ_{ch} and a wider signal bandwidth B_{TX} are considered, the wide-band echo recorded within this time contains all the contributors from the wider swath. As previously stated, the recorded signal is also properly distributed in the frequency spectrum thanks to the FScan acquisition principle. In the optimum case, the echoes completely overlap in time domain and the EWL T_{ewl} is given by:

$$T_{\mathrm{ewl,full}} = \frac{B_{\mathrm{img}}}{k_{\mathrm{r}}}, \tag{1}$$

with B_{img} being the desired target bandwidth (i.e., the range resolution) and k_{r} the transmitted chirp modulation rate. It is worth to notice that this is a first-order approximation, as it accounts neither for the rule according to which the beam direction changes with transmit frequency, nor the actual imaging geometry with the nonlinear dependency between range echo time and antenna look angle. However, this allows for a better generalization of the FScan principle to subsequent discussions and future implementations.

In conventional SAR imaging, the swath width and range resolution, and thus the bandwidth of the transmit signal, are typically considered as input parameters determined by specific mission requirements, while the chirp length is determined by the trade-off between the instrument duty cycle and the desired noise equivalent sigma zero (NESZ), with limitations imposed by the timing constraints of the radar transmit events and nadir echoes. Also in the case of the FScan mode, we consider the swath width and bandwidth (i.e., range resolution) as input parameters. In this scenario, the chirp length becomes the only parameter to be determined, ensuring that the relevant scene contributions of the received signals across the swath arrive at the receiver quasi simultaneously, as depicted in Figure 1. This is possible as the employed chirp pulse has both a wide bandwidth and a longer duration with respect to a conventional SAR mode. As a result, the received echo from each targeted point on ground within the swath is wider in bandwidth and longer in time. By considering the EWL accordingly, this condition leads to record the backscatter information introducing some overlap in time domain between two neighboring targets, with the capability to distinguish them in range/frequency domain thanks to the peculiar FScan characteristic of illuminating the area with a variable center frequency.

In the following subsections we describe the basic dependency between the chirp length and the resulting swath width for an FScan system (Section II-A). The implications for the definition of the echo window length are discussed, together with timing constraints for an X-band system in TerraSAR-X like orbit. (Section II-B).

A. Time-Frequency Diagrams

In order to visualize and better clarify the characteristics of an FScan system, Figure 2 depicts the time-frequency diagrams for three different operating modes: the traditional

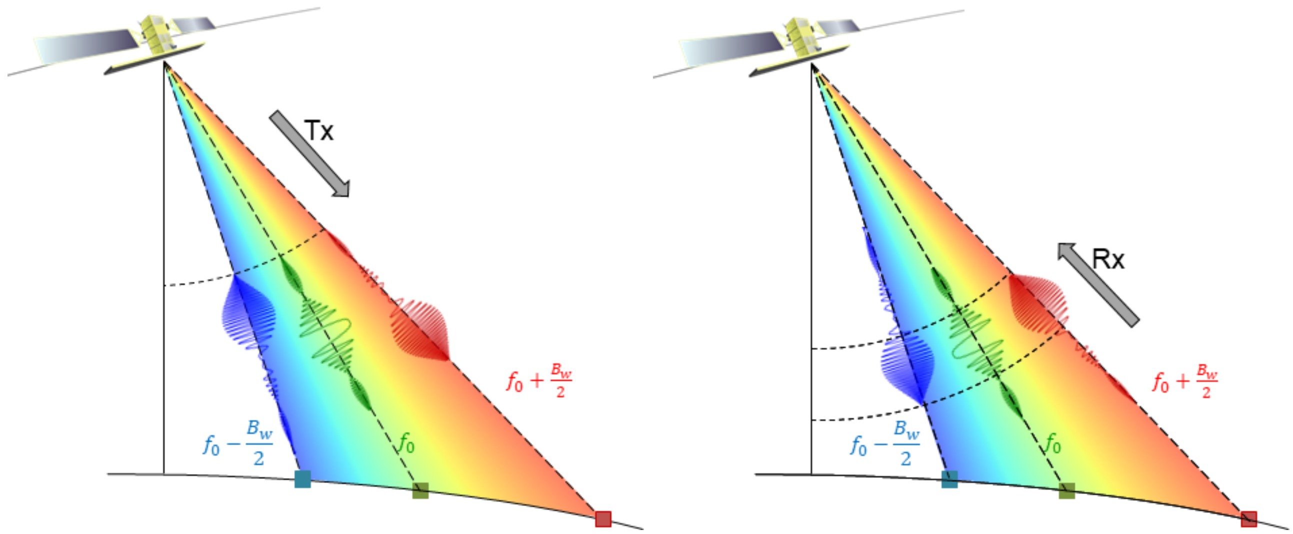

(a) Transmission (b) Reception

Fig. 1: The FScan imaging principle: (a) the linearly frequency-modulated transmit pulse is weighted by the dispersive frequency dependent antenna pattern to illuminate different areas across the swath with different frequencies; (b) on receive, the main signal components arrive quasi simultaneously at the antenna.

stripmap mode (Figure 2(a)), the FScan mode with fully overlapped echoes in time domain (Figure 2(b)) and a generalized FScan mode with only partially overlapped signals in time domain (Figure 2(c)). The difference between these last two configurations is explained in the following.

In the time-frequency representation, the abscissa corresponds to the range time vector, while the ordinate refers to the range frequency vector. The grey area represents the time-frequency support for one range line, which includes all received echoes. The diagonal coloured lines represent the echoes of three reference targets in near (blue), mid (green) and far (red) range, respectively. The extension (i.e., the duration in time and the corresponding spectral support) corresponds to the chirp length τ_{ch} along the abscissa and the chirp bandwidth B_{TX} along the ordinate. For the three cases depicted in Figure 2(a)-(c), the swath width and range resolution of the sensor are assumed to be identical. In the first case (Figure 2(a)), the target bandwidth B_{img} and the transmit bandwidth B_{TX} are equivalent, as expected for a conventional stripmap acquisition mode. By increasing the chirp duration (Figure 2(b) and Figure 2(c)), the required B_{img} can be recorded by reducing the EWL (T_{ewl}) thanks to the longer echoes received from the target and the capability to distinguish between them in the frequency domain. At this point, it becomes clear that the chirp duration τ_{ch} directly determines the required echo window length T_{ewl}.

To further illustrate this concept, the change of the center frequency is hereby assumed to be proportional to the travel time/slant range, even though, in reality, an additional modulation is expected in presence of an underlying topography and, as stated for (1), the nonlinear dependency between echo window length, beam pointing direction and range frequency. Nevertheless, in terms of center frequency variation, such a non-linearity can be considered to be much smaller than the oversampling factor of the radar and can be therefore reasonably neglected. Two numerical examples are shown in Appendix B and recommendations are given on how to overcome such a non-linear effect or the potential influence of topography.

With an initial design goal to minimize T_{ewl} as much as possible, the radar must operate with large chirp lengths. This last condition (i.e., minimization of T_{ewl}) is defined as the *fully overlapped FScan* mode and, as introduced earlier, it is depicted in Figure 2(b), leading to the following condition:

$$\tau_{\text{ch,full}} = \frac{2(r_{\text{far}} - r_{\text{near}})}{c_0\left(1 - \dfrac{B_{\text{img}}}{B_{\text{TX}}}\right)} = \frac{T_{\text{swath}}}{1 - \dfrac{B_{\text{img}}}{B_{\text{TX}}}}, \tag{2}$$

where T_{swath} is the desired swath width (converted to two-way travel time), B_{TX} the bandwidth of the transmitted chirp and B_{img} the available range bandwidth for each target, which determines the range resolution of the SAR image.

The resulting chirp duration $\tau_{\text{ch,full}}$ is much larger than in conventional SAR systems and it might not be practically feasible because of a potential constraint in the sensor duty cycle or due to timing constraints. As an alternative, one may consider only a partial overlap of the received radar echoes. We refer to this configuration as the *fixed chirp length FScan mode* (or partially overlapped) and its time-frequency support is depicted in Figure 2(c). The expression of the echo window length T_{ewl} in this case is directly related to the selected chirp length τ_{ch}:

$$T_{\text{ewl}} = \begin{cases} T_{\text{swath}} - \tau_{\text{ch}}\left(1 - 2\frac{B_{\text{img}}}{B_{\text{TX}}}\right) & \tau_{\text{ch}} < \tau_{\text{ch,full}} \\ \\ \tau_{\text{ch}} - T_{\text{swath}} & \tau_{\text{ch}} > \tau_{\text{ch,full}}. \end{cases} \tag{3}$$

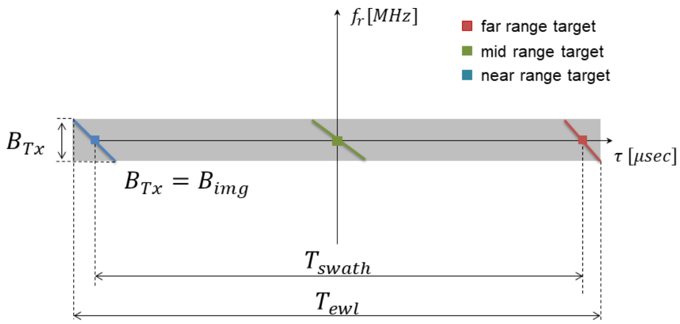

(a) Stripmap mode

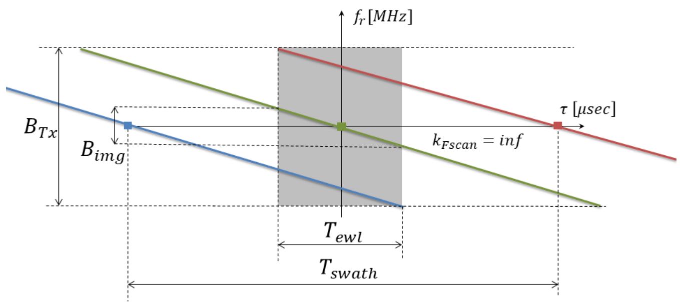

(b) fully overlapped FScan mode

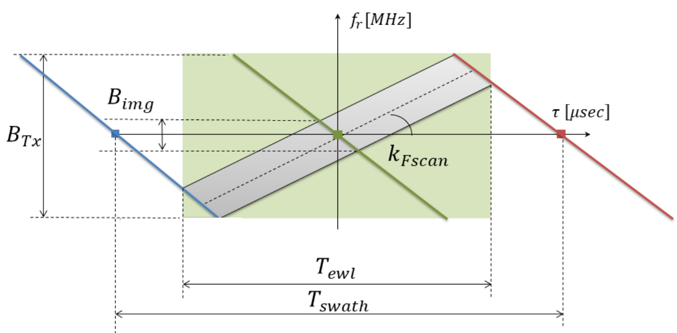

(c) fixed chirp length FScan mode

Fig. 2: Time-frequency diagrams for three exemplary targets placed in near (blue), mid (green) and far (red) range, in stripmap (a) and FScan modes (b)-(c). The minimization of the echo window length T_{ewl} is achieved by means of large chirp length τ_{ch}, leading to the *fully overlapped FScan* mode (b). On the other hand, a trade-off exists between chirp length and echo window length, as it is observed for the *fixed chirp length FScan mode* (partially overlapped) (c).

In the above equation the upper case refers to a chirp length which is shorter with respect to the fully overlapped case $\tau_{\mathrm{ch,full}}$, resulting in the partially overlapped FScan mode. The lower case, on the other hand, represents the condition in which the chirp length is larger than $\tau_{\mathrm{ch,full}}$, hence resulting in a *more than fully overlapped case*. This latter solution is not depicted in Figure 2 for the sake of brevity, but may be beneficial for the longer illumination time of the target, resulting in an improved signal-to-noise ratio (SNR). In a different context, where, for example, the driving system parameter is represented by the maximum transmit peak power, this option becomes very attractive. Nevertheless, we do not provide further detail in this paper as this case refers to a different system scenario (i.e., not a high-resolution wide-swath).

For the *fixed chirp length FScan mode*, the time-frequency signal support (grey area) becomes smaller than the area spanned by the echo window length and the sampling frequency (green rectangle). This alternative design opens up opportunities for data volume reduction by exploiting the transform coding paradigm, as discussed later in Section III.

It is important to remark that, in order to achieve a reduction of the EWL, hence optimising timing and coverage system capabilities, the sign of the adopted chirp rate needs to consider the radiation properties of the antennas. In the displayed FScan cases, the SAR antenna is assumed to illuminate the far range with higher frequencies and, as a consequence, the radar must operate with down-chirps. Equivalently, the transmission of an up-chirp pulse would require the antenna to illuminate the far range with lower frequencies (this case is not shown as it would result in a lower gain/SNR in the far range). As shown in Figure 2, the variation of the center frequency and spectral support for each target in the two FScan modes is also identical. This is a rather realistic assumption as the spectral illumination of the swath is dictated by the antenna settings and not by the choice of the specific pulse characteristics.

B. Timing Constraints

For the FScan mode, the stripmap timing condition $\tau_{\mathrm{ch}} + T_{\mathrm{ewl}} \leq \mathrm{PRI}$ translates into a maximum allowable chirp duration of:

$$\tau_{\mathrm{ch,max}} = (\mathrm{PRI} - T_{\mathrm{swath}}) \cdot \frac{B_{\mathrm{TX}}}{2B_{\mathrm{img}}}, \tag{4}$$

being PRI derived from the system pulse repetition frequency as $\mathrm{PRF} = 1/\mathrm{PRI}$.

Let us now consider the exemplary cases of a 30 km and 80 km swath width acquired at a mid range look angle of 39°. These result in an equivalent T_{swath} of 136 µsec and about 362 µsec, respectively. With a PRF of 2000 Hz, an exemplary chirp bandwidth $B_{\mathrm{TX}} = 1.2$ GHz, and $B_{\mathrm{img}} = 300$ MHz, the maximum possible chirp duration is $\tau_{\mathrm{ch,max}} = 727.8$ µsec / 274.9 µsec, while the requirement for the fully overlapped FScan mode according to (2) is $\tau_{\mathrm{ch,full}} = 181.4$ µsec / 483.4 µsec. The 80 km example shows that the fully overlapped FScan mode might become unfeasible for larger swath widths (i.e., the required time for transmitting the chirp and listening to the backscattered echo may be larger than the PRI of the system). For this reason, in the following we concentrate on the *fixed chirp length FScan mode* configuration only, i.e., the case shown in Figure 2(c).

In addition to these considerations, timing diagrams should be investigated to verify whether a specific set of FScan parameters (i.e., chirp duration, PRF) is feasible for a certain geometry (i.e., look angle and swath width). As a summary of all the above considerations, we have derived a set of nominal parameters (reported in Table I) for a quantitative evaluation of an exemplary FScan system configuration, with the sensor operating at X band and flying in a TerraSAR-X-like orbit [25], [26]. The desired azimuth resolution of $\delta_{\mathrm{az}} = 1$ m requires a Doppler bandwidth B_{d} of at least 7000 Hz. With $N_{\mathrm{az}} = 4$

TABLE I: Main system parameters for the considered FScan configuration.

Parameter	Value
Center frequency, f_0	9.8 GHz
Transmit bandwidth, B_{TX}	1200 MHz
Target bandwidth, B_{img}	300 MHz
Orbit height, h_{sat}	514 km
Antenna size (el. $\times$ az.) [15]	1.4 m $\times$ 6 m
Number of azimuth subapertures, N_{az}	4
Azimuth resolution, δ_{az}	1 m

azimuth channels the PRF can be reduced to below 2000 Hz [21], [27]. Taking these parameters as reference, one can derive τ_{ch} and T_{ewl} for the different modes depicted in Figure 2. The timing diagram for an 80 km swath at 39° look angle is presented in Figure 3, where both a conventional stripmap mode and a partially overlapped FScan mode are considered, assuming the same orbit height. For both modes a transmit duty cycle of 18% for the stripmap and 48% for the partially overlapped FScan mode has been assumed.

Transmit events are colored in red, while the compressed nadir echo for a 2 km width to account for nadir topography variations is shown in blue. As for the operational TerraSAR-X mission, we use the compressed nadir echo since it allows for more freedom in choosing the swath width and PRF settings [28]. Feasible echo window positions for achieving a swath width of 80 km are marked in green. From the diagrams it is possible to notice that the considered *fixed chirp length FScan mode* (or partially overlapped) can provide the desired swath width for PRF settings around 1500 Hz, 1750 Hz and 2050 Hz, while the stripmap and fully overlapped FScan mode fail to achieve it. Note that an azimuth resolution of 1 m requires 7000 Hz of unambiguous Doppler bandwidth. This is possible if a PRF setting within the last two feasible PRF bands (1750-2100 Hz) is considered together with the 4 receive channels (as indicated in Table I) and the MAPS recombination is applied prior to SAR image formation [9]. Several look angle regions turn out to be feasible. For example, one is centered around 4.35 ms, which corresponds to a central look angle of 35°, and another one at 3.8 ms, corresponding to a central look angle of 30°. For further insight, these two cases are considered in more detail in Appendix B. The first one assumes a PRF of 1975 Hz, which is the lowest value of the last suitable PRF region. For the 35° look angle and a constant duty cycle of 0.48% leads to a chirp length of $\tau_{\mathrm{ch}} = 243$ µs and a comparable T_{ewl} of about 240 µs. The other example is for the steeper look angle of 30° and assumes a chirp length of 100 µs and a swath width of 50 km, and it corresponds to the numerical performance evaluation presented in Section IV. The mathematical formulations provided in this section allow for the derivation of the optimized timing design for a generic FScan system, given a set of input acquisition parameters, such as orbit height, look angle, swath width, and desired image resolutions.

III. Data Volume Reduction for FScan SAR Systems

The diagram in Figure 2(c) highlights the informative signature of the recorded scene (gray area) and how it represents a sub-portion of the whole time-frequency support (green area). Starting from this, it is clear how a direct digitization and on-board storage of the entire signal support is highly inefficient, since the actual informative content occupies only a certain portion of it. Moreover, a simple subsampling of the signal would not help as the target information is spread along the entire signal bandwidth B_{TX} and would lead to aliased signal components from sidelobes of the antenna elevation beams (not shown). An inefficient storage of data on board leads to a series of drawbacks, such as coverage limitations due to overhead in the system memory or downlink capacity. The definition of efficient data volume reduction approaches is therefore of crucial importance in all SAR missions, especially for high-resolution wide-swath acquisition methods, as in the FScan case, because of the higher amount of recorded data.

On the basis of these considerations, we investigated a dedicated on-board processing of the recorded data, in order to fully assess the potentials for data volume reduction of an FScan system. In this work, we consider three different approaches for on-board implementations. Two of them feature a deramping operation, thus performing a data transformation before the encoding, while a third one implements a block-wise Fast Fourier Transform (FFT). The block scheme depicted in Figure 4 summarizes the three considered methods, highlighting the respective operational steps and procedures.

The first two approaches are both described in Section III-A since they share certain steps in common for their implementation, while the third one is presented in Section III-B. Finally, Section IV reports the corresponding performance evaluation by means of synthetic SAR scene simulation.

A. Use of Deramping Operation

Independent of the specific FScan chirp parametrization, the on-board Analog-to-Digital Converter (ADC) needs to sample the data at a rate which is higher than the transmit pulse bandwidth B_{TX}, in order to avoid aliasing effects. As introduced in the previous section, the recorded data need to be conveniently transformed in order to achieve an efficient reduction of the resulting data volume. A simple way to do so is to perform a *deramping* operation directly on the raw data samples (i.e., in time domain). This consists of a multiplication of the data by a complex exponential $e^{j\varphi_{\mathrm{D}}}$ with linearly varying frequency, defined as

$$e^{j\varphi_{\mathrm{D}}} = \cos\varphi_{\mathrm{D}} + j\sin\varphi_{\mathrm{D}} \tag{5}$$

where its phase φ_{D} is expressed as follows

$$\varphi_{\mathrm{D}} = -\pi \cdot k_{\mathrm{FScan}} \cdot \left(\frac{(r - r_{\mathrm{mid}}) \cdot 2}{c_0}\right)^2 \tag{6}$$

In the above equation, r and r_{mid} refers to the considered range position and to the one in the center of the swath, respectively. This allows one to properly vertically shear the information space , resulting in a time-frequency support

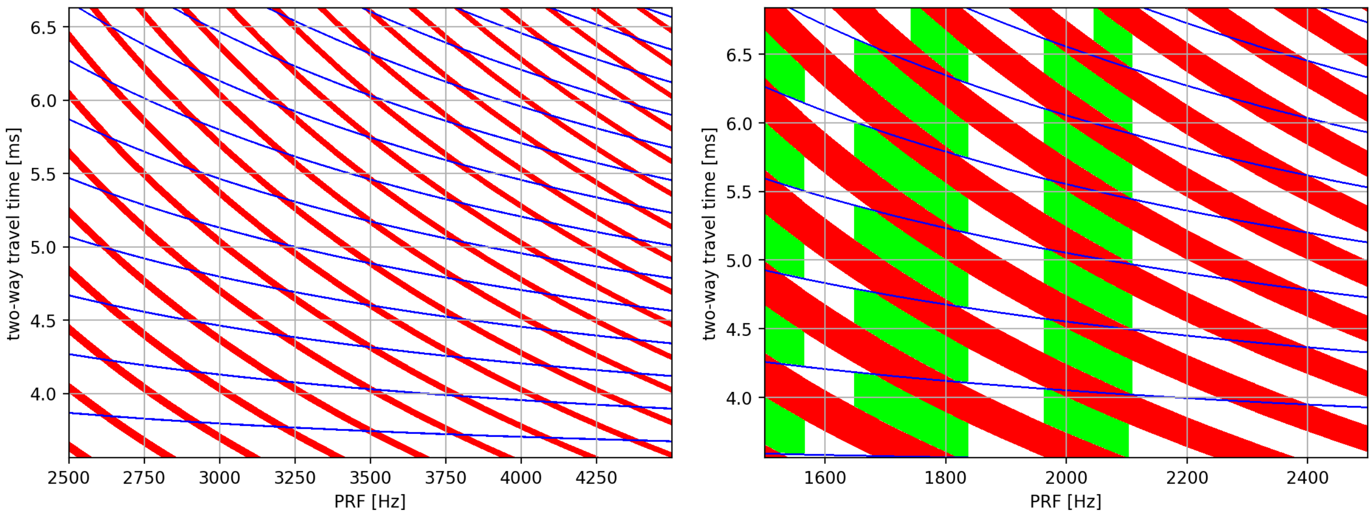

(a) TerraSAR-X (b) *fixed chirp length FScan mode*

Fig. 3: Timing diagrams for a conventional stripmap TerraSAR-X system (a) and partially overlapped FScan mode (b). The red areas correspond to transmit events and blue lines to range compressed nadir echoes, while the green regions indicate feasible PRF values to cover a swath width of 80 km at 39° look angle (the corresponding travel time is of about 4.53 ms). In (a) there is no value of PRF which allows for acquiring the entire scene, on the other hand, in (b) three suitable PRF ranges around 1550 Hz, 1750 Hz and 2050 Hz satisfy the timing constraints. Constant duty cycles were assumed, 18% in (a) and 48% in (b).

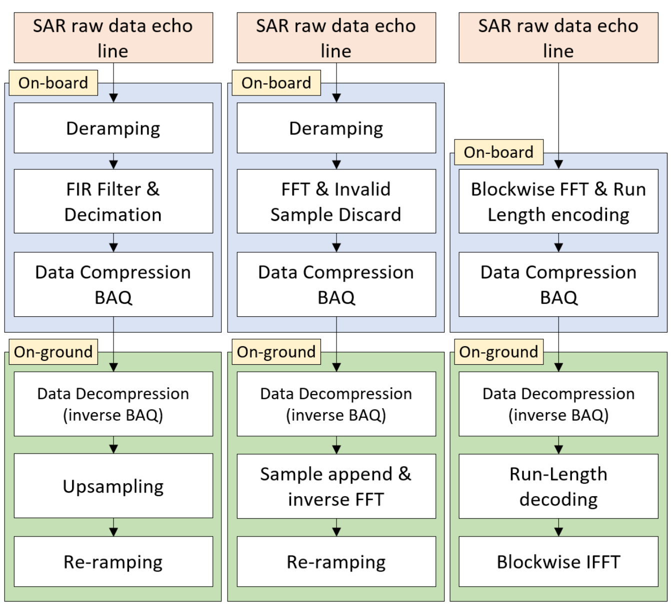

(a) (b) (c)

Fig. 4: Three possible implementations for data volume reduction in FScan systems, (a) Deramping, low-pass filtering and standard (time-domain) quantization (DerFilt), (b) Deramping and quantization in frequency domain (DerFFT) and (c) featuring a block-frequency block-adaptive quantization (BF-BAQ).

similar in shape to the one obtained for a classical stripmap mode and depicted in Figure 5. After this operation the total bandwidth of the signal can be reduced as the spectral support of the target over time is not spread anymore along the whole transmitted bandwidth. The instantaneous bandwidth of the

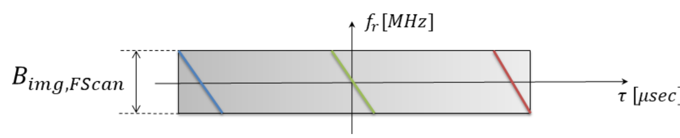

Fig. 5: Time-frequency diagram for the fixed chirp length FScan case depicted in Figure 2(c) after applying the deramping operation.

signal after the deramping operation is expressed as:

$$B_{\mathrm{img,FScan}} = B_{\mathrm{img}} \cdot \left(1 - \frac{k_{\mathrm{FScan}}}{k_{\mathrm{r}}}\right), \tag{7}$$

with

$$k_{\mathrm{FScan}} = -\frac{B_{\mathrm{TX}} - B_{\mathrm{img}}}{T_{\mathrm{swath}} - \tau_{\mathrm{ch}}\left(1 - \frac{B_{\mathrm{img}}}{B_{\mathrm{TX}}}\right)}. \tag{8}$$

The effect of deramping on the FScan signal is depicted in Figure 6, where the raw data spectrum of a single range line is represented, together with its deramped version and the relevant system parameters B_{img} and $B_{\mathrm{img,FScan}}$ (green and black vertical lines, respectively). At this point one could consider to apply the quantization of the data in either time or frequency domain, as described in the following.

1) Time Domain Quantization: After performing the deramping operation, the implementation of a low-pass filter (LPF) together with a decimation operation allows for a reduction of both the bandwidth and the sampling rate. The steps of this approach are reported in Figure 4(a). Such a solution, referred to as deramping and filtering (DerFilt), requires a significant computational complexity for the implementation of a finite impulse response (FIR) filter. In Section IV, an estimation of the number of operations, which are required to

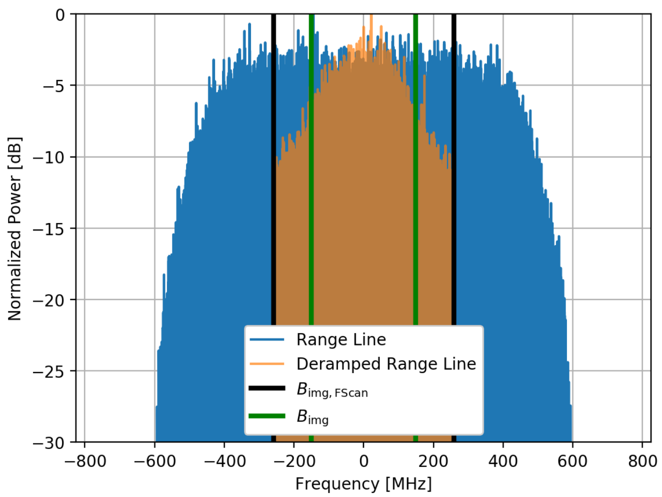

Fig. 6: The effect of deramping on FScan raw data spectrum: in blue the recorded signal with bandwidth B_{TX}; in orange the same signal (a single range line) after the deramping operation. The black and green lines delimit the $B_{\mathrm{img,FScan}}$ and B_{img}, respectively. The considered system parameters are summarized in Table I.

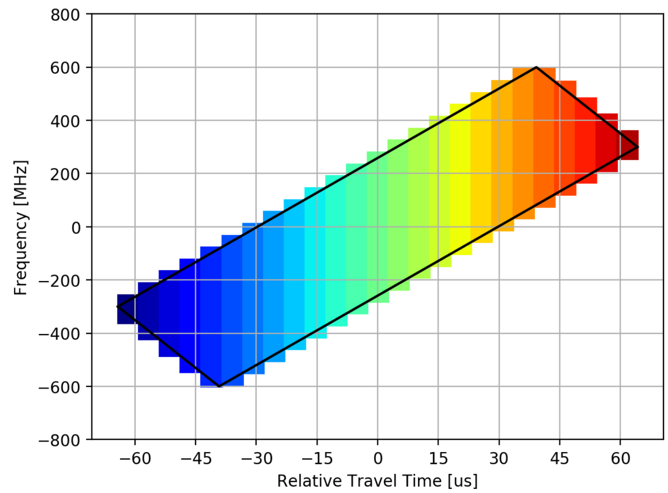

Fig. 7: Time-frequency diagram of FScan raw data, where the target information content support is identified by the black rhomboid. N_b=25 blocks are hereby considered. Each coloured rectangle extends between f_{min} and f_{max} according to (10).

filter the data with a set of possible FIR filters is provided, for different lengths (i.e., number of taps).

2) Frequency Domain Quantization: After the deramping operation, the resulting raw data can be alternatively quantized in the frequency domain. This approach is described in the block diagram in Figure 4(b). By applying a Fast Fourier Transform on the entire range line, it is possible to filter out (i.e., discard) the samples belonging to the frequency support which are located outside the bandwidth $B_{\mathrm{img,FScan}}$. For this case the BAQ operates on the range samples (separately on in-phase and quadrature components) transformed in the frequency domain. This approach has been proposed for efficient quantization on single-channel stripmap SAR systems in [29], [30], and in this paper it is referred in Figure 4(b) and in the following as deramping + FFT (DerFFT) approach.

As visible in Figure 6, the deramped signal is quantized only in between the two black lines identifying the boundaries of $B_{\mathrm{img,FScan}}$. This operation corresponds to an ideal filtering but also requires a significant computational complexity, since the FFT operation has to be performed on the entire range line, which, in the case of FScan operation in wide swath, can result in a considerably large number of samples. It is worth to mention that for this case, the green triangles in the top-left and bottom-right corners of Figure 2(c) will be included in the signal after the deramping as they will be sheered inside $B_{\mathrm{img,FScan}}$. In view of the definition of data volume reduction methods, this may represent a limiting factor as these portions of the time-frequency spectrum are related to targets lying outside the imaged swath. Another important issue concerns how the data support is actually affected by quantization in the range spectrum domain: the encoding method is not performed along the range dimension but along the frequency one, possibly raising concerns about the representation quality of the targets in presence of variation in the SAR backscatter of the imaged scene.

All these considerations are treated in detail in Section IV-B, where both the computational burden and the performance adaptivity in presence of backscatter inhomogeneities of the target are analyzed.

B. Block-Frequency BAQ (BF-BAQ)

In this section we propose an alternative solution which operates in the frequency domain for the efficient encoding of FScan raw data: the Block-Frequency BAQ (BF-BAQ). For its implementation it does not require any deramping operation, which would imply, as described in the previous section, a vertical shear of the spectrum dependent on the range position. The idea is to avoid the quantization of the whole signal support represented by the green area in Figure 2(c), but to concentrate only on that part of the frequency support which actually contains informative target spectral signatures (corresponding to the gray area in Figure 2(c)).

Accordingly, the block scheme in Figure 4(c) summarizes the foreseen processing steps. For this purpose, the received signal within the EWL in the time domain is opportunely divided in N_b blocks and for each of them the FFT is calculated. This initial processing step is equivalent to a short-time Fourier transform (STFT) in order to represent the raw data in a time-frequency domain. The target information is concentrated in a specific portion of the bandwidth as function of the target position in range: as the range position increases, the target information is mapped into intervals at lower frequency. By representing each block in the transformed (frequency) domain, it becomes clear that the non-informative content can be excluded by simply performing a run-length encoding.

Figure 7 shows a visual representation of the proposed concept where the informative content of each block is depicted with different colors and N_b=25 blocks have been considered.

The target information content is limited to a smaller number of samples as the color suggests (approximately one third) with respect to the original bandwidth support. All samples lying outside the colored area can be disregarded a priori by relying on the knowledge of the specific system parameters for the location of the frequency blocks. As depicted in Figure 2(c), the relationship between the time and frequency support is fixed to key system parameters which are further detailed in the following. For removing the samples which do not carry informative content, we are interested in identifying the frequency components corresponding to a specific instant in time within the received EWL, thus defining the time-frequency relationship of the FScan data. The following formulas summarize the criteria for the definition of the target information space in the frequency domain (i.e., the different blocks): for a given instant of relative round-trip time (t_{RRTT}), its corresponding bandwidth is delimited by the frequencies f_{min} and f_{max}, defined as:

$$f_{min} = \begin{cases} -\frac{B_{\mathrm{TX}}}{2} + \left(\frac{T_{\mathrm{EWL}}}{2} + t_{\mathrm{RRTT}}\right) \cdot k_{\mathrm{r}} + B_{\mathrm{img}}, \\ \quad \text{for } t_{\mathrm{RRTT}} < -\frac{T_{\mathrm{EWL}}}{2} - \frac{B_{\mathrm{img}}}{k_{\mathrm{r}}} \\ t_{\mathrm{RRTT}} \cdot k_{\mathrm{FScan}} - \frac{1}{2} B_{\mathrm{img,FScan}}, \text{ elsewhere} \end{cases} \tag{9}$$

$$f_{max} = \begin{cases} \frac{B_{\mathrm{TX}}}{2} - \left(-\frac{T_{\mathrm{EWL}}}{2} + t_{\mathrm{RRTT}}\right) \cdot k_{\mathrm{r}} + B_{\mathrm{img}}, \\ \quad \text{for } t_{\mathrm{RRTT}} > \frac{T_{\mathrm{EWL}}}{2} + \frac{B_{\mathrm{img}}}{k_{\mathrm{r}}} \\ t_{\mathrm{RRTT}} \cdot k_{\mathrm{FScan}} + \frac{1}{2} B_{\mathrm{img,FScan}}, \text{ elsewhere.} \end{cases} \tag{10}$$

Once the frequency blocks have been identified, a standard BAQ is applied to each block and to the in-phase and quadrature components of the complex samples, separately. For all the considered simulations we utilized blocks of 128 samples for the definition of the BAQ settings, as this value is the nominal one used in other spaceborne SAR systems (such as the TerraSAR-X and TanDEM-X missions).

If we now consider a fixed bitrate for quantizing each data block, a significant reduction of the average bitrate can be achieved by opportunely avoiding the quantization of those portions of the spectral support which are outside of the considered blocks. The resulting average bitrate can be expressed as:

$$R_{\mathrm{eq}} = \frac{R \cdot (S_{\mathrm{data}} - S_{\mathrm{disc}})}{S_{\mathrm{data}}}, \tag{11}$$

where R stands for data rate measured in bits per sample used in the quantization. S_{data} and S_{disc} correspond to the total number of samples in the data frequency support and to the number of samples which have been discarded, respectively. Clearly, the larger S_{disc}, the lower the resulting data rate to be handled by the system.

One can also think of a solution in which the deramping is employed before the BF-BAQ in order to avoid the "staircase" relationship of the time-frequency spectrum when FFT blocks are comuputed (i.e., which may be non optimal). This option has led to negligible gain in the performance in our simulations, for this reason, we have decided to consider the straightforward application of the BF-BAQ, so to ideally reduce the number of operations necessary to implement the deramping on board.

Another possibility could also be to perform the deramping operation and followed up by an efficient state-of-the-art implementation of a simple FIR filter in order to diminish the overall bandwidth (following the concept of the DerFilt approach). After that, a proper signal decimation (to discard redundant samples after the LPF) followed by the implementation of the BF-BAQ (with an appropriate update of (9) and (10) on the new time-frequency spectrum displacement due to the deramping operation) could benefit in terms of number of operations from the reduced bandwidth of the signal (i.e., less computational burden required by the block-wise FFT). It is worth pointing out that, in this case, an optimized filter design together with an FFT on a reduced number of samples after decimation may lead to a more optimized implementation in terms of computational burden and hardware realization. Nevertheless, this approach (which we could refer to as DerFiltFFT), does not bring any advantage in terms of data volume reduction with respect to the BF-BAQ due to the non-idealities of the time-domain low-pass filter, which would result in an increase of the effective bandwidth to be processed, therefore it will not be further investigated in this paper.

IV. Performance Evaluation

In order to assess the FScan data compression performance and, in particular, to evaluate the proposed solutions for raw data quantization and data volume reduction, we implemented the FScan acquisition mode in a simulation environment. The goal is to provide a performance assessment of the different quantization approaches which have been presented in Section III. In this section, a set of performance metrics is presented, which represent key parameters for data volume reduction in SAR raw data quantization. Later on, the structure of the simulation is defined and specific scenarios are investigated considering different SAR backscatter distributions (Section IV-B), as well as a variable bit allocation for quantization to further improve the resulting performance (Section IV-C).

A. Performance Metrics

For SAR systems, a key quality indicator to measure the impact of quantization errors on SAR data is the signal-to-quantization noise ratio (SQNR), which is expressed as:

$$\mathrm{SQNR} = \frac{\sigma_s^2}{\sigma_q^2}, \quad \text{with} \quad q = s - s_q. \tag{12}$$

The above equation represents the SQNR as the ratio between the variance of the uncompressed signal s and the variance of the quantization error q, which is in turn defined as the difference between the non-quantized signal s and its quantized, distorted version s_q. It is important to notice that the SQNR can be used to derive the overall signal-to-noise ratio of the considered system [31]. The SNR can be expressed as the

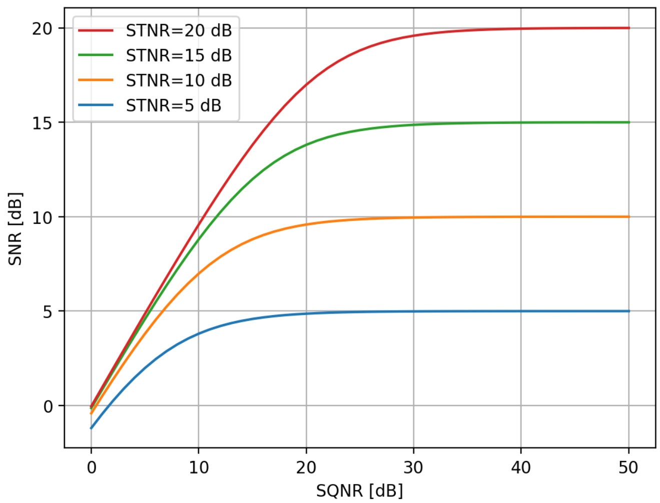

Fig. 8: SNR as function of the SQNR for a given set of signal-to-thermal noise ratio (STNR) values.

ratio of the radar backscatter σ^0 and the sum of the thermal noise σ^2_{TN} and of the quantization noise σ^2_{QN} as follows:

$$SNR = \frac{\sigma_0}{\sigma^2_N} = \frac{\sigma_0}{\sigma^2_{TN} + \sigma^2_{QN}}, \tag{13}$$

which leads to

$$SNR^{-1} = STNR^{-1} + SQNR^{-1}, \tag{14}$$

where STNR represents the signal-to-thermal noise ratio. We have calculated the total SNR depending on the SQNR for a set of STNR values and the resulting plot is depicted in Figure 8. In this way it is possible to estimate, starting from a given thermal noise and SAR backscatter, the required value of SQNR (and, in turn, of the minimum bitrate) to satisfy a certain SNR requirement.

In addition to the SQNR, another important parameter for performance evaluation is the achieved data volume reduction ($DVR_{\%}$), which is defined as

$$DVR_{\%} = \left(1 - \frac{\overline{R}}{R_{\mathrm{BAQ}}}\right) \cdot 100, \tag{15}$$

being $\overline{R}$ the overall average bitrate for a given quantization technique and R_{BAQ} the overall bitrate employed for a standard BAQ to achieve the same value of SQNR. From this, if $\overline{R}$ is smaller than R_{BAQ}, $DVR_{\%}$ would result in a positive value, which basically represents the amount of memory saved with respect to the reference BAQ method.

In our performance investigation we focused our attention on the DerFFT and BF-BAQ solutions (depicted in Figure 4(b) and Figure 4(c), respectively). This choice is driven by the fact that the DerFilt method (depicted in Figure 4(a)) would imply us to impose constraints in terms of filter design which will result in a performance which may not be consistent if a different system configuration is selected. Moreover, in terms of data volume reduction, the performance is theoretically bounded to the techniques featuring optimum filtering (i.e., FFT). Nevertheless, we have performed a comparison of the three proposed quantization methods in terms of computational complexity.

We estimated the number of operations required for performing their characterizing time and frequency-domain steps. For this, we can assume the operation to be applied to both the complex components of the data. Regarding quantization in time-domain, we consider a set of possible lengths of the LPF (number of taps). Since the time discrete filtering of a digital signal is implemented by means of a convolution operation after the deramping, a first general estimation of the required number of on-board operations for this approach, represented with the big $\mathcal{O}$ notation, is given by:

$$\mathcal{O}_{\mathrm{DerFilt}} \propto N_{\mathrm{EWL}} + N_{\mathrm{EWL}} \cdot (2 \cdot F_t - 1), \tag{16}$$

where F_t is the number of taps of the considered filter and N_{EWL} indicates the number of samples within the echo window length, and is defined as

$$N_{\mathrm{EWL}} = T_{\mathrm{ewl}} \cdot f_s, \tag{17}$$

being f_s the sampling frequency. The first N_{EWL} term in (16) stands for the deramping operation (which is equivalent to N_{EWL} multiplications), N_{EWL} in the second term represents all the samples for which the filter output needs to be computed. It is worth pointing out that if, in a specific case of implementation of this method, one should consider a decimation before the filtering operation, N_{EWL} in the second term must be substituted with the number of samples kept after the decimation, leading to a further reduction of required operations. Moreover, system specific symmetrical low pass filter realizations could also contribute in reducing the number of operations [32]. An analog processing method may considerably reduce the overall number of operations, but, as a drawback, it will inevitably limit the flexibility of the onboard system. For this reason we have considered a digital filter.

The other two proposed approaches for data volume reduction include instead the implementation of a FFT transformation, in one case for the entire sample length of the EWL (as in Figure 4(b), after the deramping for the DerFFT method) and, in the case of the BF-BAQ described in Figure 4(c), for one block of the sampled EWL, while the operation is repeated multiple times. The number of operations required for the DerFFT on the entire range line is given by:

$$\mathcal{O}_{\mathrm{DerFFT}} \propto N_{\mathrm{EWL}} + N_{\mathrm{EWL}} \cdot \log_2 N_{\mathrm{EWL}}. \tag{18}$$

Also in this case, the first N_{EWL} term stands for the necessary deramping operation. In this paper we have assumed a Radix2 FFT implementation, being the one offering a good flexibility on the signal length (less zero-padding required). If the encoding design on a specific system should be considered, one has the possibility to implement the FFT in a more efficient way depending on the available system scenario and data format.

If the signal is divided into N_b blocks, as for the BF-BAQ, and multiple FFTs are performed on a smaller number of samples, the number of operations $\mathcal{O}_{\mathrm{BF-BAQ}}$ becomes:

$$\begin{aligned} \mathcal{O}_{\mathrm{BF-BAQ}} &\propto N_b \cdot \frac{N_{\mathrm{EWL}}}{N_b} \cdot \log_2 \frac{N_{\mathrm{EWL}}}{N_b} \\ &\propto N_{\mathrm{EWL}} \cdot \log_2 \frac{N_{\mathrm{EWL}}}{N_b}. \end{aligned} \tag{19}$$

By comparing (18) and (19) it is possible to observe that the block-wise FFT (BF-BAQ) requires a smaller amount of operations with respect to the DerFFT on the entire length. Following the $DVR_{\%}$ representation, the Computational Cost Reduction ($CCR_{\%}$) can be derived, which gives information on the amount of computational reduction in percentage by employing the block-wise FFT (BF-BAQ) with respect to the deramping followed by the FFT on the entire EWL signal (DerFFT):

$$CCR_{\%} = 100 \cdot \left(1 - \frac{\mathcal{O}_{\mathrm{BF-BAQ}}}{\mathcal{O}_{\mathrm{DerFFT}}}\right). \tag{20}$$

B. Simulation Results

We have implemented the methods described in Figure 4 and in the previous sections, and carried out simulations in order to assess their performance. The developed simulator includes the complete FScan mode emulation along the range dimension (i.e., by considering the antenna pattern (AP) and the specific FScan weighting), with the capability to perform encoding of raw data using the proposed techniques. The block representation of the simulator structure is depicted in Figure 9, while different scenarios have been investigated in the following subsections.

1) Uniform SAR backscatter: We carried out the first set of simulations assuming a homogeneous SAR backscatter to evaluate the overall performance. We generated the raw data assuming normal distribution for their real and imaginary part, zero-mean with constant variance σ^2 and according to the FScan parameters presented in Table I for a *fixed chirp length FScan mode* (depicted in Figure 2(c)). The encoding/decoding is then performed for both the techniques featuring deramping and FFT (DerFFT, Figure 4(b)) and BF-BAQ (Figure 4(c)). For comparison, we considered data quantization through the state-of-the-art BAQ as well, in order to properly derive the $DVR_{\%}$ performance metric described in (15). After that, we compressed the data in range and we filtered it with a Hamming filter characterized by $\alpha = 0.6$ [33], as shown in Figure 9. Finally, we evaluated the performance metrics introduced in Section IV-A (SQNR, $DVR_{\%}$, $CCR_{\%}$).

For the DerFFT technique, we refer to the spectrum of the signal (and its deramped version) shown in Figure 6, where one can observe the data before being quantized. The spectrum of the deramped signal is indeed not flat, which is due to the weight introduced by the antenna pattern in the FScan weighting step. This effect is modeled in the simulation with a Hanning type low pass filter (with α=0.7) as no real antenna pattern model is considered. At this point the spectrum of the signal is BAQ-quantized in the frequency domain disregarding the samples lying outside the $B_{\mathrm{img,FScan}}$ limits. It is important to remember that in a real scenario the samples lying outside these boundaries are not zero but are equal to the backscatter value from areas outside the imaged swath, allowing this method to act as a range ambiguity and noise filter as well [16].

The manipulation of the data during the described processing steps according to the BF-BAQ method can be seen in Figure 10 in the form of a time-frequency diagram: the coloured parts of the blocks represent the useful signal support which is actually quantized (similarly to Figure 7). The black parts (vertical solid lines) refer to the samples which are discarded from the signal support.

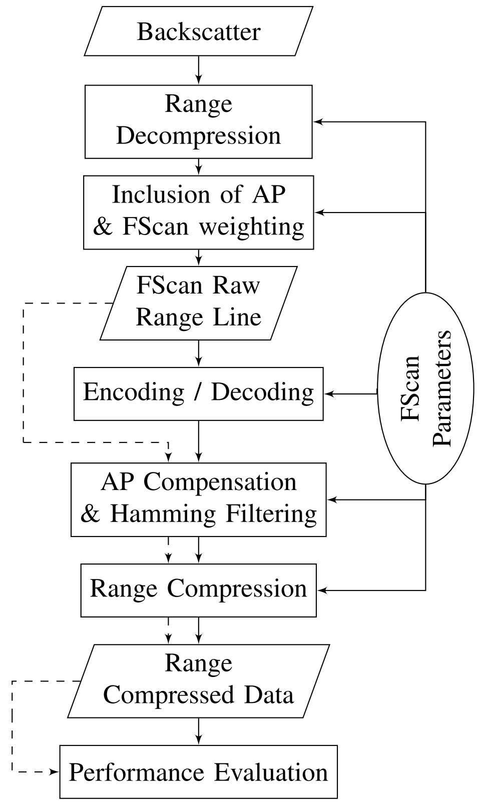

Fig. 9: Block diagram showing the processing steps taken into account in the simulation structure. The dashed line represents the uncompressed version of the data which is used as reference in the performance evaluation block.

TABLE II: Number of required operations for the different methods presented in Figure 4.

Technique		Number of Operations [1e6]
DerFilt	F_t	
	12	4.62
	15	5.77
	21	8.08
	25	9.63
	51	19.64
	100	38.90
DerFFT		1.21
BF-BAQ	N_b	
	5	0.88
	10	0.82
	25	0.74
	50	0.69
	80	0.65
	100	0.63

The overall number of required operations for the DerFFT, BF-BAQ and the DerFilt options are reported in Table II, where the considered number of taps F_t and of frequency blocks N_b are listed as well. By considering the overall number of operations, it is clear that the employment of the low-pass filter in time domain requires a significant number of opera-

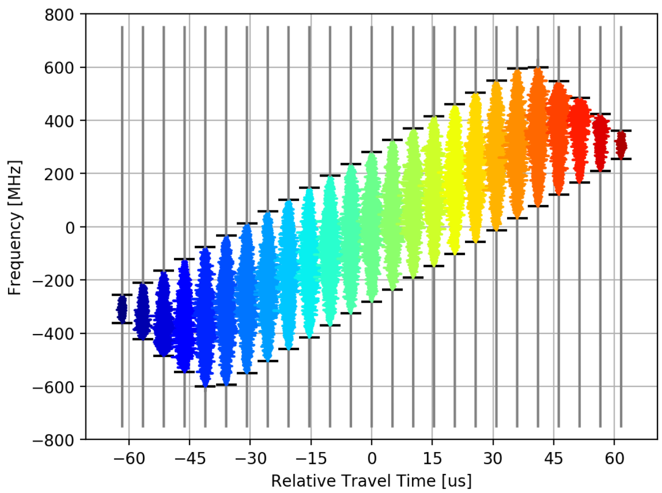

Fig. 10: Time-frequency representation of BF-BAQ quantized data for the case of $N_b = 25$. Each vertical line depicts an FFT-block, the coloured part refers to the quantized informative content (i.e., the power of the corresponding raw data spectral block) and the black vertical part to the disregarded non-informative content. The horizontal marks delimit the informative signal support, and can be derived a priori from the FScan acquisition parameters.

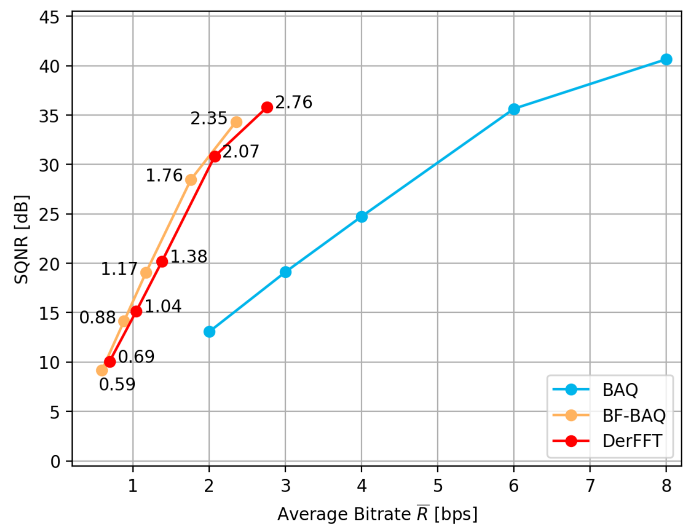

Fig. 11: SQNR as function of the average bitrate $\overline{R}$ calculated on range-compressed data for the BAQ (light blue curve), BF-BAQ assuming $N_b = 50$ blocks (orange) and for the DerFFT technique (red curve). The R_{eq} value, which takes into account the discarded samples, is reported close to the corresponding SQNR measurement.

tions with respect to the other techniques. Moreover, a low-pass filter for this specific case should satisfy very precise cut-off requirements due to the high bandwidth span of the signal to be filtered (for which a considerable amount of taps could be required). One could argue that, despite its high computational cost, low-pass filtering operation is easier to be implemented on-board by means of state-of-the-art FPGAs. However, the FFT operation, although requiring a more specific processor for its on-board implementation, can also be easily handled on current spaceborne systems, making the on-board FFT a likewise viable solution [34]. The reported observations should be intended as general comments, nonetheless they do not account for a real-case scenario where a specific hardware architecture may be available, hence making more preferable one of the proposed techniques with respect to the other ones. It is also possible to notice that the employment of block-wise FFT requires less operations with respect to the full range line FFT, hence resulting in an increased $CCR_{\%}$. Starting from these considerations, and by utilizing the formulation in (11), we calculated the SQNR on range-compressed data for all the proposed solutions, by considering different average bit rates. For the BF-BAQ case, we considered an exemplary $N_b = 50$ blocks. The results are shown in Figure 11.

Here, the R_{eq} value, introduced in (11), is derived for the solutions employing sample discard (DerFFT and BF-BAQ). This value is then used for the calculation of $DVR_{\%}$, by directly substituting it into (15), assuming $\overline{R} \simeq R_{\mathrm{eq}}$.

The detailed summary of the results, including the investigated set of N_b, is reported in Table III. The performance of BF-BAQ improves as the considered number of blocks N_b increases. This is caused by the fact that a smaller amount of

TABLE III: Results for distributed target simulation. R is the bitrate used to quantize each raw data sample, $\overline{R}$ is the average bitrate after discarding the non-useful samples after proper data transformation, R_{BAQ} is the BAQ rate which achieves the same encoding quality in terms of SQNR. $DVR_{\%}$ and $CCR_{\%}$ are the resulting data volume reduction and computational complexity reduction (w.r.t. DerFFT), respectively.

Technique	R [bps]	$\overline{R}$ [bps]	R_{BAQ} [bps]	$DVR_{\%}$	$CCR_{\%}$
DerFFT					
	3.0	1.04	2.2	52.7	
	4.0	1.38	3.0	54.0	
	6.0	2.07	4.8	56.9	
BF-BAQ					
N_b=5	3.0	1.31	2.2	40.5	27.0
	4.0	1.74	3.1	43.9	
	6.0	2.62	4.8	45.4	
N_b=10	3.0	1.07	2.2	51.4	31.8
	4.0	1.43	3.1	53.9	
	6.0	2.14	4.8	55.4	
N_b=25	3.0	0.93	2.2	57.7	38.1
	4.0	1.24	3.0	58.7	
	6.0	1.86	4.7	60.4	
N_b=50	3.0	0.88	2.1	58.1	42.9
	4.0	1.17	3.0	61.0	
	6.0	1.76	4.5	60.9	
N_b=80	3.0	0.86	2.1	59.1	46.2
	4.0	1.15	2.9	60.3	
	6.0	1.73	4.2	58.8	
N_b=100	3.0	0.86	2.1	59.1	47.7
	4.0	1.14	2.8	59.3	
	6.0	1.72	3.8	54.7	

blocks (e.g. $N_b = 5$) implies a less accurate quantization of the spectrum, i.e., the "shape" of the spectral support as function of time is not well reconstructed. On the other hand, by selecting a larger number of blocks, the block division is able to better follow the shape of the time-frequency relationship (can be observed in Figure 7).

At the same time, the larger the number of blocks, the smaller the number of samples contained in each block, leading to a coarser spectral representation. One can notice that the encoding capabilities of the DerFFT in terms of $DVR_{\%}$ are slightly worse than the BF-BAQ with number of blocks of about $N_b = 50$. It is also important to consider that the BF-BAQ achieves this encoding quality employing a lower number of operations, which results in a $CCR_{\%}$ of 42.9% for this specific case.

When defining the number of blocks, a particular attention should be given to the fact that an FFT is going to be performed on each single data block. The number of blocks N_b implicitly defines the number of samples of the block (N_{EWL}/N_b), which also represents the frequency resolution of the FFT. A small block size would result in a coarser frequency representation, i.e., a less accurate filtering of the target support spectrum. We have derived a theoretical maximum number of blocks for a given system by assuming that the frequency resolution should be at least as small as the diagonal of the exceeding part of the block with respect the target information depicted in Figure 7, resulting in the following:

$$\frac{B_{\mathrm{TX}}\ N_b}{N_{\mathrm{EWL}}} \leq k_{\mathrm{FScan}} \frac{t_{\mathrm{EWL}}}{N_b}, \tag{21}$$

solving for N_b one obtains

$$N_b \leq \sqrt{t_{\mathrm{EWL}} \cdot \frac{k_{\mathrm{FScan}} \cdot N_{\mathrm{EWL}}}{B_{\mathrm{TX}}}}. \tag{22}$$

By considering our system parameters, we obtain that N_b has to be lower than 400. As we are considering a Radix-2 FFT, the number of samples contained in each block should be considered as close as possible to a power of 2 in order to avoid performing zero padding on a large part of the signal. In fact, since the minimization of the data volume represents the main goal, a zero padding prior to the FFT would also mean to perform an interpolation of the signal in the frequency domain. It is worth mentioning that these considerations should also be taken into account in the context of noise filtering and terrain topography dependence (further described in Appendix B), where a sufficient performance can be achieved without increasing too much N_b, i.e., an extremely large number of blocks does not lead to a better performance. For our case scenario we have verified that selecting N_b in the order of about 70 blocks results in the best performance in terms of achievable DVR.

2) Non-uniform SAR backscatter: As introduced in Section II and shown in Figure 2(c), for the case of *fixed chirp length FScan* the target responses are superimposed but they occupy different portions of the range spectrum. This effect and the implications for data volume reduction are discussed in the following scenario, which comprises a simulation where the illuminated swath is not homogeneous and presents two

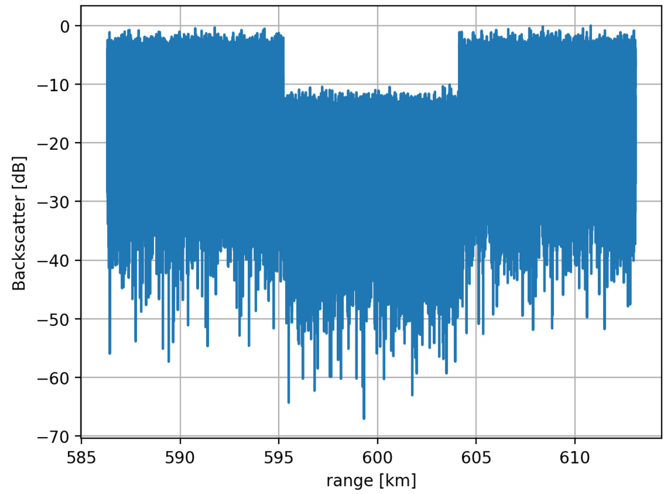

Fig. 12: Non-uniform SAR backscatter distribution along the swath considered in the simulation, showing a discontinuity of 10 dB in the profile.

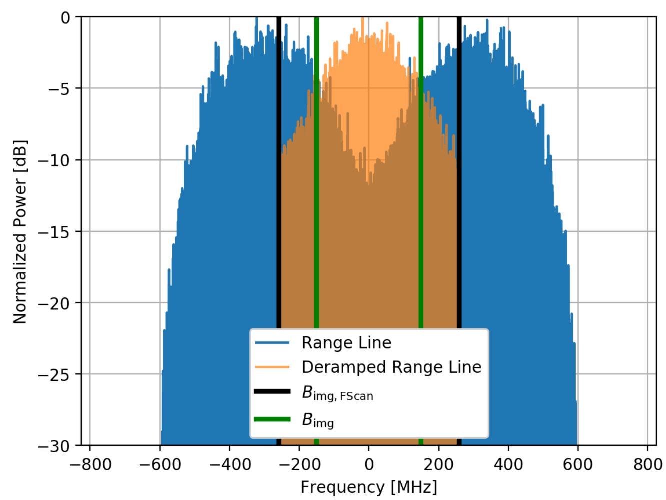

Fig. 13: Raw data spectrum of one FScan range line characterized by the non-uniform backscatter shown in Figure 12 (in blue) and the same spectrum after the deramping operation (in orange). The two black lines represents the $B_{\mathrm{img,FScan}}$ limits.

discontinuities in the SAR backscatter profile, as shown in Figure 12.

The difference in terms of SAR backscatter between the central part of the swath and the near and far range is of 10 dB. In Figure 13, the spectrum of a raw data range line for this scenario is shown in blue, while the spectrum of the target after the deramping operation is depicted in orange. It is of interest to compare this plot with the spectrum for the case of homogeneous backscatter distribution in Figure 6 (i.e., constant power along the range dimension). One can notice that the energy of the signal of the raw data (blue) presents high values at higher and low frequencies (corresponding to near and far range, respectively), while a lower amount of energy is concentrated in the central part of the spectrum (corresponding to the mid range). This behaviour is consistent

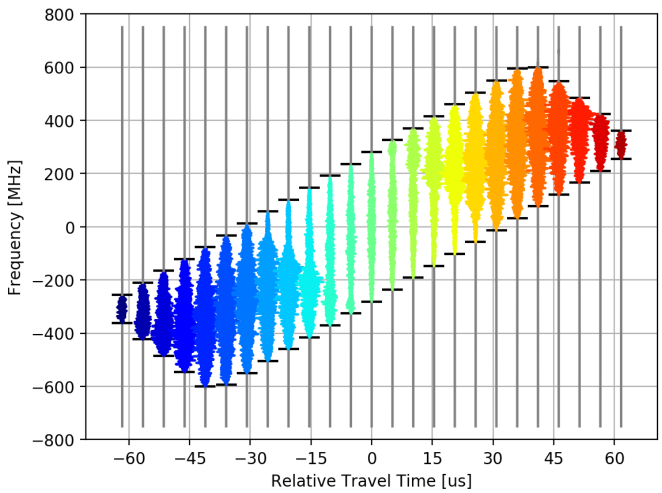

Fig. 14: Time-frequency representation of a raw data range line acquired in FScan mode and further processed according to the proposed BF-BAQ (in the example N_b= 25) for the non-unifrom target simulation scenario. Each vertical line corresponds to a considered block, while the coloured part refers to the corresponding raw signal power spectrum (normalized) and the black one to the disregarded non-informative content.

with the target statistics illustrated in Figure 12.

Differently, the distribution of the deramped signal looks more similar to the one for the uniform backscatter case. This is due to the fact that, by performing a single FFT on the full deramped range line, all the signal components are represented in a single overlay within the $B_{\mathrm{img,FScan}}$. This results (also for this case) in the inclusion in the target signal of samples outside the imaged swath, which are lying in the top-left and bottom-right corners of Figure 2(c). Moreover, the bell shape, caused by the effect of the antenna pattern, is visible as well (as for Figure 6). In conclusion, the subdivision in blocks of the signal performed by the BF-BAQ is expected to better maintain the spectral components separated along the range dimension, an aspect which is further detailed in the following.

In Figure 14, the time-frequency representation for the profile shown in Figure 12 is depicted (as done in Figure 10 for the case of homogeneous backscatter), where the central blocks (i.e., for range frequencies around 0) correspond to the lower backscatter components of the received signal. The detailed performance obtained for different simulation assumptions is reported in Table IV, and consistent results are observed with respect to the homogeneous backscatter case (summarized in Table III).

Moreover, for this analysis, it is worth looking at the quantization performance along the range dimension as well. The SQNR for the range-focused data is depicted in Figure 15 for different data compression schemes: the standard BAQ and the proposed DerFFT and BF-BAQ (the latter with $N_b = 5$ (a) and $N_b = 50$ (b)). For this representation we have considered bitrate values which achieve a comparable performance in terms of $DVR_{\%}$, i.e., by observing Table IV. As it can be clearly noticed, the resulting performance

TABLE IV: Results for non-uniform target simulation. The same performance parameters as in Table III are considered.

Technique	R [bps]	$\overline{R}$ [bps]	R_{BAQ} [bps]	$DVR_{\%}$	$CCR_{\%}$
DerFFT					
	3.0	1.04	2.2	52.7	
	4.0	1.38	3.0	54.0	
	6.0	2.07	4.8	56.9	
BF-BAQ					
N_b=5	3.0	1.31	2.2	40.5	27.0
	4.0	1.74	3.1	43.9	
	5.0	2.62	4.8	45.4	
N_b=10	3.0	1.07	2.2	51.4	31.8
	4.0	1.43	3.1	53.6	
	5.0	2.14	4.8	55.4	
N_b=25	3.0	0.93	2.2	57.7	38.1
	4.0	1.24	3.0	58.7	
	5.0	1.86	4.7	60.4	
N_b=50	3.0	0.88	2.1	58.1	42.9
	4.0	1.17	2.9	59.7	
	5.0	1.76	4.2	58.1	
N_b=80	3.0	0.86	2.1	59.1	46.2
	4.0	1.15	2.9	60.3	
	5.0	1.73	4.1	57.8	
N_b=100	3.0	0.86	2.0	57.0	47.7
	4.0	1.14	2.7	57.8	
	5.0	1.72	3.7	53.5	

of each technique is not constant over the range dimension and follows the variation in the backscatter, especially for the BAQ and the DerFFT cases. Only the BF-BAQ is able to maintain a good adaptivity along the whole scene extension when a larger number of blocks are considered (i.e., $N_b = 50$). The performance degradation in presence of inhomogeneities of the SAR backscatter is known as low-scatter suppression phenomenon: if two targets with different magnitude responses are overlapping in the raw data domain, the stronger signal is better represented, while the lower one is significantly distorted (as described in [35] and [36]). The average SQNR values within the central region (also delimited by the two vertical lines in Figure 15 (a) and (b)) are reported in Table V for the different encoding techniques.

The results confirm that the BF-BAQ is able to better preserve the information especially in the low-backscatter region with respect to time-domain BAQ and the DerFFT.

C. Variable Bitrate Allocation

In all the previous simulations, the bitrate R has been kept constant for the quantization of the raw data samples (i.e., for DerFFT and BF-BAQ the bitrate employed along the spectrum was not varying for all samples). Raw SAR data is usually modeled as a zero-mean distributed Gaussian process. However, it is possible to see from the spectrum resulting from of both DerFFT and BF-BAQ approaches (Figure 6 and Figure 13, respectively) that the raw data signal is characterized by a non-uniform power distribution in frequency. In particular, the observed bell-shape of the signal spectrum is due to the modulation of the antenna pattern, resulting in a larger power contribution concentrated in the middle part of the spectrum. This effect is anyhow compensated later on at processing stage and, typically, a Hamming windowing is applied afterwards in order to improve the signal quality, at the cost of a certain resolution loss [37]. The resulting spectrum is characterized by

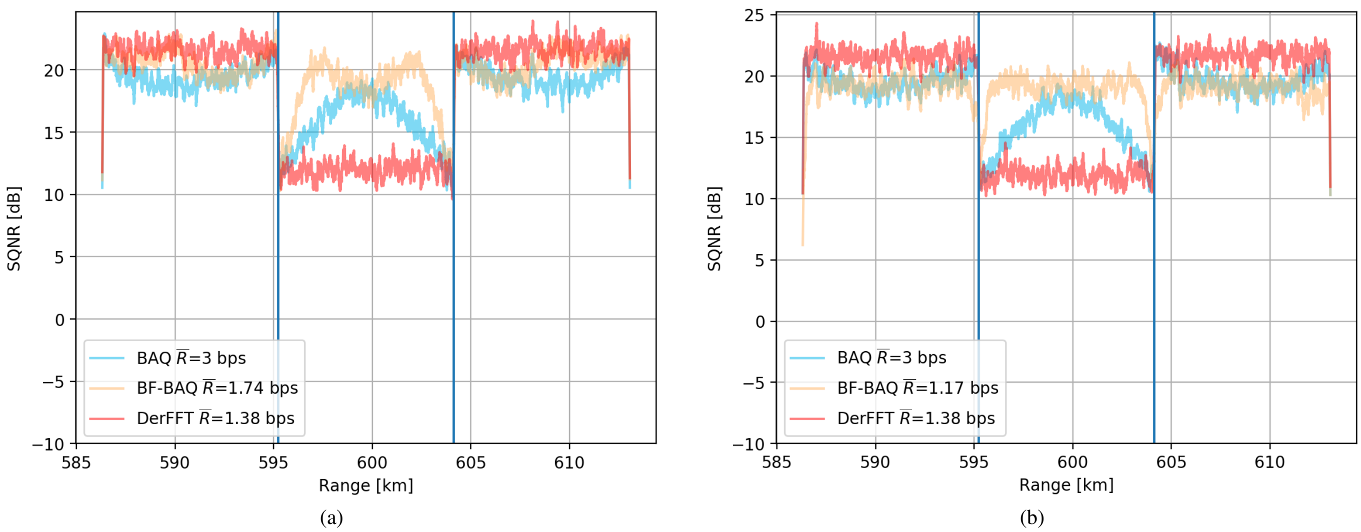

Fig. 15: SQNR along the range dimension for $R = 3$ bits/sample for the BAQ (in light blue), and $\overline{R}$ for the proposed DerFFT and BF-BAQ, evaluated for the average rate $\overline{R}$ providing the same average performance as the BAQ. The BF-BAQ is analyzed in (a) with $N_b = 5$ and in (b) with $N_b = 50$. The two vertical lines delimit the low-backscatter area, for which the corresponding average SQNR values are reported in Table V.

a bell-like shape as a consequence of the Hamming filtering. Such characteristics give the opportunity for a more efficient bitrate allocation which allows for a further performance improvement (or, equivalently, for data reduction capabilities).

In [29], a power-based bit allocation was introduced for SAR systems, which was similarly applied to multichannel SAR systems in [21]. The authors exploited transform coding [38], [39], based on the different power statistics of the received channels, in order to derive a non-uniform bitrate selection for the different spectral (Doppler) sub-bands and so to improve the overall encoding performance. In this work, we have implemented this approach for both the DerFFT and the BF-BAQ techniques, in order to better exploit the non-uniform power distribution in the range dimension exhibited by the raw signal spectrum for both approaches, as shown in Figure 6 and in each block of Figure 7.

In [21], the authors define the bitrate allocation by considering the power distribution of the focused SAR signal. This means that the signal components, which will be filtered out at processing stage, are encoded with a lower amount of bits or, in some cases, even disregarded. To apply the same concept to the FScan scenario, we have considered the power distribution of the range compressed signal after the Hamming filtering. In this way, it is possible to spend less bits for quantizing portions of the spectrum which will be attenuated by the Hamming filter itself. At the same time more bits are allocated for the portion of the spectrum which will be better preserved during the processing (i.e., the central part as shown in Figure 6).

In Figure 16, the flow chart of the simulator implementing the variable bitrate allocation is depicted. In this case, we have considered as reference power distribution one of the non-quantized signal after the range compression, thus including antenna pattern correction and Hamming filtering.

In order to implement a variable bitrate allocation, the signal to be quantized must be divided in K sub-bands in the

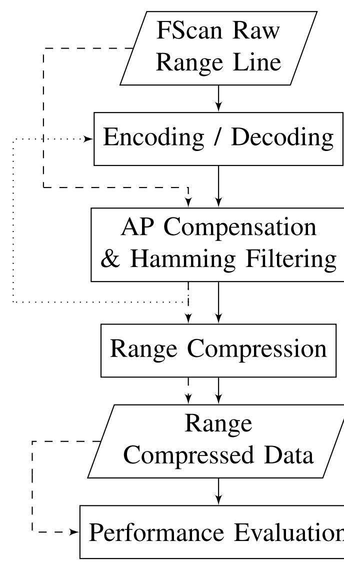

Fig. 16: Block scheme of the simulation structure with optimized bitrate allocation based on the spectral power distribution of the focused SAR data. The dotted line represents the filtered reference signal from which the power distribution is calculated.

frequency domain. The power contribution of each frequency sub-band, denoted as σ_k^2, is proportional to the integral of the Dirichlet kernel over the bandwidth of the signal. It is expressed as:

$$\sigma_k^2 = \frac{P_k}{K^2} \int_{-R_{\text{img,FScan}}/2}^{R_{\text{img,FScan}}/2} \left| \frac{\sin\left(\pi K \frac{f + f_s(K/2-k)/K}{f_s}\right)}{\sin\left(\pi \frac{f+f_s(K/2-k)/K}{f_s}\right)} \right|^2 df, \tag{23}$$

where K stands for the considered number of sub-bands and P_k is the power associated to the transform coefficient. The

TABLE V: SQNR of the low-backscatter region of Figure 15. R is the bitrate used to quantize each raw data sample, $\overline{R}$ is the average bitrate after discarding the non-useful samples after proper data transformation. The SQNR is calculated on the area delimited by the blue lines in Figure 15.

Technique	R **[bps]**	$\overline{R}$ [bps]	**SQNR [dB]**
BAQ			
	3.0	3.00	15.72
	4.0	4.00	21.08
	6.0	6.00	31.75
DerFFT			
	3.0	1.04	6.88
	4.0	1.38	11.87
	6.0	2.07	22.49
BF-BAQ			
N_b=5	3.0	1.31	13.21
	4.0	1.74	18.22
	6.0	2.62	28.68
N_b=10	3.0	1.07	13.04
	4.0	1.43	18.05
	6.0	2.14	28.34
N_b=25	3.0	0.93	13.71
	4.0	1.24	18.68
	6.0	1.86	28.94
N_b=50	3.0	0.88	13.79
	4.0	1.17	18.70
	6.0	1.76	28.55
N_b=80	3.0	0.86	13.44
	4.0	1.15	18.39
	6.0	1.73	28.08
N_b=100	3.0	0.86	13.33
	4.0	1.14	18.18
	6.0	1.72	26.35

bitrate allocated to each spectral sub-band is the result of the average target R with the addition of a ΔR_k term, which can be positive or negative and is directly related to σ_k^2. ΔR_k can be expressed as:

$$\Delta R_k = \frac{1}{2} \cdot \log_2 \frac{\sigma_k^2}{\left[\prod_{l=1}^{K} \sigma_l^2\right]^{1/K}}. \tag{24}$$

The resulting rate R_k is therefore derived as:

$$R_k = R + \Delta R_k = R + \frac{1}{2} \cdot \log_2 \frac{\sigma_k^2}{\left[\prod_{l=1}^{K} \sigma_l^2\right]^{1/K}}. \tag{25}$$

In the above equation, the power ratio results in a positive term if the considered k-th block has a larger power distribution component with respect to the geometric mean of the power components calculated for all blocks. On the other hand, the ΔR_k term can also be negative if the corresponding k-th channel carries a less significant amount of information. In any case, the overall average rate $\overline{R}$ and defined as:

$$\overline{R} = \frac{1}{K} \sum_{k=1}^{K} R_k, \tag{26}$$

remains equal to the nominal (integer) rate R.

All that considered, we repeated the set of simulations and assessed the performance by including the described variable bit rate allocation. In particular, we concentrated on the homogeneous target scenario. The considered number of sub-bands consists of a minimum of 3 to a maximum of 71. This last rather large value has been included in the analysis in order to identify a sort of upper bound of the performance.

For the BF-BAQ case, in which the signal is already limited in terms of number of samples (e.g. for the case of $N_b = 50$ the informative part is composed of about 850 samples for the blocks lying in the central part of swath), the sub-bands are selected by grouping samples at multiple of BAQ blocks (i.e., 128 samples). As an example, if 13 sub-bands are considered, the minimum signal length is 13×128=1664 samples. This suggests that, in some extreme cases where both a high number of blocks and a large number of sub-bands are considered, this subdivision may not be feasible due to an insufficient number of samples for each block. Another observation concerns the actual capability to realize fractional rates: taking into account that the considered BAQ scheme is able to compress to integer quantization rates (e.g. 2 bps/3 bps/4 bps) only, in [40] a fractional bitrate is realized by properly toggling integer rates between adjacent range lines (alternatively, additional blocks can be added such as e.g., an entropy coder, as it is done for the implementation of the FDBAQ [19]). After SAR focusing, the resulting performance is equivalent to the case as if the average (non-integer) bitrate was used.

In this contribution this concept has been applied by toggling integer bitrates between BAQ blocks along the range dimension. A limitation of this approach arises when implementing the variable bitrate: if, as in some cases, only a limited number of blocks is available (a few per sub-band), it is not possible to perfectly obtain the desired bitrate. This aspect should be carefully considered when interpreting the results. As an example, if a spectral channel contains only 5 BAQ blocks (i.e., $5 \times 128 = 640$ samples) and the required bitrate is 3.8 bps, the 5 blocks will be quantized with 4, 4, 3, 4 and 4 bits/sample, whose average is exactly 3.8 bits/sample but the same target bitrate could not be realized if, e.g., only 4 BAQ blocks were available. Thus, the desired bitrate can be effectively implemented only if sufficient BAQ blocks are available within the corresponding frequency samples block.

After performing the focusing operation, the information and the error introduced by quantization will be smeared as result of the convolution with the range chirp, averaging the rate to 3.8 bits/sample on the overall range line [40].

We measured the gain in terms of $DVR_{\%}$ improvement with respect to the uniform bit allocation case. A summary of the results of the described investigation for variable bitrate is reported in Table VI, which includes the rate variation ΔR_k, defined in (24), respectively.

From the results, it is possible to notice that a marginal gain in terms of $DVR_{\%}$ with respect to the uniform bitrate is indeed present for the DerFFT technique. For the DerFFT technique the entire range line has been divided in sub-bands, resulting in a consistent implementation of variable rate thanks to the large amount of samples available.

TABLE VI: Data volume reduction, expressed in percentage increase by means of variable bitrate with respect to constant bitrate for the DerFFT and BF-BAQ techniques. ΔR_k is the bitrate variation for each of the considered channel reported in (24). R represents the average bitrate on the informative support of the signal (i.e., the quantized part). For the BF-BAQ, the cases of block lengths (N_b = [5, 10, 15]) which allows for effective variable bitrate implementation are reported.

sub-bands K	ΔR_k	R	$DVR_{\%}$ **Gain [%]**			
			DerFFT	N_b=5	N_b=10	N_b=25
3	[-0.37, +0.68, -0.31]	3	0.00	0.37	3.95	1.30
		4	0.19	0.00	2.11	0.71
5	[-0.92, +0.44, +0.86, +0.43, -0.81]	3	3.29	12.05	9.62	4.72
		4	2.96	10.56	6.79	3.08
7	[-1.19, -0.01, +0.68, +0.91, +0.68, -0.01, -1.06]	3	2.85	14.32	10.86	7.05
		4	3.60	13.58	9.30	4.30
13	[-1.49, -0.79, -0.16, +0.34, +0.69, +0.88, +0.96, +0.87, +0.66,+0.32, -0.18, -0.78, -1.32]	3	2.06	18.85	13.38	6.24
		4	3.74	14.58	10.18	4.06
71	[-1.57, ... +0.99, ... -1.63]	3	2.53	17.55	0.41	0.00
		4	3.82	14.50	0.00	0.00

The results for the BF-BAQ also showed a slight improvement with respect to the constant bitrate case, e.g., 13 sub-bands with 5 blocks up to 15-18% more of data reduction, which verifies the effectiveness of the variable bitrate allocation to improve data volume reduction capabilities. Simulations with larger N_b ([50, 80, 100]) have not been carried out due to the abovementioned constraint with the non-sufficient number of BAQ blocks to properly implement the variable spectral rate allocation. For the other cases, the exact value of R_k has not been achieved (for the abovementioned reason), resulting in a slightly different value of R with respect to the constant bit allocation case. This would result in inconsistent comparison between the two approaches. Therefore, in such situation we have edited the bit allocation iteratively in order to match the R value of the uniform bit allocation case. This allows to coherently compare the two methods as the overall number of bits employed for quantizing the signal are just the same. For some cases in which N_b is relatively small (e.g., $N_b = 5$), a considerable gain is observed.

This investigation suggests that, for the considered FScan system, a power spectral-based bit allocation may contribute to improve the overall performance if the considered number of BF-BAQ blocks are limited. In particular, the BF-BAQ configuration with $N_b = 80$ and constant bitrate achieves similar performance with respect to a configuration with smaller N_b and variable bit allocation. One should consider that the implementation of a variable bit allocation brings more complexity into the system, and the performance requirement of considering a smaller N_b is also translated in a greater FFT complexity as the blocks are made up of more samples.

V. Conclusions and Outlook

In contrast with conventional stripmap SAR systems, future SAR missions will be capable to acquire wider swaths at finer resolution. In this paper, we investigated acquisition design aspects and novel approaches for data volume reduction for the Frequency Scan (FScan) SAR mode. In the first part of our contribution, we described the FScan principle and the corresponding mathematical formulation. In particular, we analyzed in detail a representative case of *fixed chirp length FScan mode* (or partially overlapped) option capable to perform high-resolution wide-swath acquisitions. Together with the main system and FScan parameters, we presented two novel solutions for data volume reduction, named Deramping FFT (DerFFT) and Block-Frequency (BF)-BAQ. We evaluated the effectiveness of the proposed methods through a set of simulations in which we considered various performance indicators on different simulated scenarios. Additionally, we also developed and investigated a more elaborated bitrate allocation scheme based on the spectral power distribution of the frequency blocks, identifying the target informative content.

We proved that the proposed methods provide comparable performance but outperform a standard BAQ. In particular, the DerFFT technique features a deramping operation followed by an FFT, while the BF-BAQ performs a blockwise FFT, which allows for more robustness in case of non-uniform backscatter distributions and requires significantly less operations with respect of the DerFFT. Moreover, the deramping operation included in the DerFFT does not provide an optimum filtering of the data support in the near and far range positions. On the other hand, the BF-BAQ is able to achieve a data volume reduction of 60% with respect to the state-of-the-art BAQ, implying the lowest increase of complexity in terms of required onboard operations with respect to the other considered methods. From all the investigated scenarios, the best performing configuration for the assumed FScan system parameters is the BF-BAQ with 80 blocks. A variable bitrate allocation approach based on distribution of the spectral power components introduced by the antenna pattern weighting is also discussed, showing an increase in terms of performance, in particular for the options employing a smaller number of blocks (e.g., DerFFT and BF-BAQ operating at $N_b = 5$). Nevertheless, for the optimal case of the BF-BAQ with 80 blocks, variable bit allocation could not be implemented due to insufficient BAQ blocks. This last option with uniform bit allocation shows comparable results to variable bit allocation conditions in which a consistent gain is observed, where a lower number of operations and therefore lower onboard complexity are required.

For the design of an FScan SAR system, the main findings of the present research should be taken into consideration, which can be summarized as follows: the selection of N_b for the BF-BAQ should be properly defined a priori and the bitrate should be carefully selected in order to balance data volume reduction and overall signal quality representation. A possible approach to bitrate selection can depend on the acquired scene characteristics, as proposed in [31]. In particular, when fractional bitrates are targeted, it is essential to verify that the resulting data blocks are large enough to effectively implement the target fractional bitrate (and avoid rounding effects).

The potentials of FScan as candidate in future spaceborne SAR missions are promising: its capability to acquire large swath widths (in this case we considered a swath width of 80 km from TerraSAR-X like orbit geoematry) with reduced echo window length represents a concrete solution to the limitation of conventional SAR acquisition modes. In this paper we focused the data compression performance analyses on the *fixed chirp length FScan mode*. If, on the other hand, the Fully Overlapped mode (depicted in Figure 2(b)) is the method of choice, we want to emphasize that for homogeneous scenarios there is no particular benefit with respect to BAQ in terms of data volume reduction due to the abscence of oversampling in the time frequency domain.

Future works will extend the investigation on real SAR backscatter scenes, where a more detailed and complete performance assessment could be implemented, taking into account, e.g., additional parameters such as the ambiguity ratio, noise equivalent sigma zero and the resulting interferometric product quality. In addition, more elaborated bit allocation schemes can be derived by combining the target response in frequency domain along multiple range lines, in combination with target performance-optimized bitrate allocation strategies.

Appendix A
Derivation of Relevant Equations

For the derivation of (2) we refer to the fully overlapped FScan case in Figure 2(b). The expression for T_{swath} is:

$$T_{\mathrm{swath}} = \tau_{\mathrm{ch,full}} - \frac{B_{\mathrm{img}}}{k_r}, \tag{A.1}$$

where k_r is the chirp rate (negative for a down-chirp):

$$k_r = -\frac{B_{\mathrm{TX}}}{\tau_{\mathrm{ch,full}}}. \tag{A.2}$$

After combining the two previous equations, one obtains the required chirp duration $\tau_{\mathrm{ch,full}}$ for the fully overlapped FScan case for a given swath width T_{swath}, i.e. (2):

$$\tau_{\mathrm{ch,full}} = \frac{T_{\mathrm{swath}}}{1 - \frac{B_{\mathrm{img}}}{B_{\mathrm{TX}}}}. \tag{A.3}$$

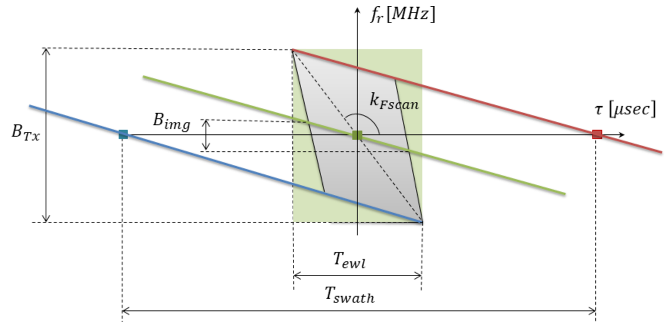

Fig. A.1: Time Frequency diagram for the so-called "more than fully overlapped" FScan case.

The echo window length for this same case is:

$$T_{\mathrm{ewl,full}} = \frac{B_{\mathrm{img}}}{k_r} = \tau_{\mathrm{ch,full}} \cdot \frac{B_{\mathrm{img}}}{B_{\mathrm{TX}}} = \frac{T_{\mathrm{swath}}}{\frac{B_{\mathrm{TX}}}{B_{\mathrm{img}}} - 1}. \tag{A.4}$$

For the more general partially overlapped/fixed chirp length case with reference to Figure 2(c), T_{ewl} is derived as follows:

$$\begin{aligned} T_{\mathrm{ewl}} &= T_{\mathrm{swath}} - 2 \cdot \frac{\tau_{\mathrm{ch}}}{2} + 2 \cdot \frac{B_{\mathrm{img}}}{k_r} \\ &= T_{\mathrm{swath}} - \tau_{\mathrm{ch}} + 2 \cdot \frac{B_{\mathrm{img}}}{B_{\mathrm{TX}}} \tau_{\mathrm{ch}} \\ &= T_{\mathrm{swath}} - \tau_{\mathrm{ch}} \left(1 - 2 \cdot \frac{B_{\mathrm{img}}}{B_{\mathrm{TX}}}\right). \end{aligned} \tag{A.5}$$

The second case of (3), where $\tau_{\mathrm{ch}} > \tau_{\mathrm{ch,full}}$, is easily derived from Figure A.1, resulting in:

$$T_{\mathrm{ewl}} = \tau_{\mathrm{ch}} - T_{\mathrm{swath}}. \tag{A.6}$$

Further, (4) is derived by inserting (3) into the condition $\tau_{\mathrm{ch}} + T_{\mathrm{ewl}} < \mathrm{PRI}$. With reference to Figure 2(b) we also derive k_{FScan} in (8). The abscissa and ordinate of the central dashed line of the gray signal support are $T_{\mathrm{ewl}} + \frac{B_{\mathrm{img}}}{k_r}$ (k_r is negative) and $B_{\mathrm{TX}} - B_{\mathrm{img}}$, respectively. Thus,

$$k_{\mathrm{FScan}} = \frac{B_{\mathrm{TX}} - B_{\mathrm{img}}}{T_{\mathrm{ewl}} + \frac{B_{\mathrm{img}}}{k_r}} \tag{A.7}$$

and, by inserting T_{ewl} from (3) and using $k_r = -\frac{B_{\mathrm{TX}}}{\tau_{\mathrm{ch}}}$, one obtains:

$$\begin{aligned} k_{\mathrm{FScan}} &= \frac{B_{\mathrm{TX}} - B_{\mathrm{img}}}{T_{\mathrm{swath}} - \tau_{\mathrm{ch}} \left(1 - 2 \cdot \frac{B_{\mathrm{img}}}{B_{\mathrm{TX}}}\right) + \frac{B_{\mathrm{img}}}{k_r}} \\ &= \frac{B_{\mathrm{TX}} - B_{\mathrm{img}}}{T_{\mathrm{swath}} - \tau_{\mathrm{ch}} \left(1 - \frac{B_{\mathrm{img}}}{B_{\mathrm{TX}}}\right)}. \end{aligned} \tag{A.8}$$

By performing the deramping, the inherent modulation of the signal needs to be removed. This corresponds to the multiplication of a chirp with modulation rate k_{FScan}.

As a consequence, the bandwidth of a single target is increased from the initial bandwidth B_{img} by the amount $k_{\mathrm{FScan}}\frac{B_{\mathrm{img}}}{B_{\mathrm{TX}}}\tau_{\mathrm{ch}} = -k_{\mathrm{FScan}}\frac{B_{\mathrm{img}}}{k_r}$, becoming

$$B_{\mathrm{img,FScan}} = B_{\mathrm{img}} \cdot \left(1 - \frac{k_{\mathrm{FScan}}}{k_r}\right). \tag{A.9}$$

Noting that the instantaneous bandwidth of the signal is $B_{\mathrm{img,FScan}}$ (the deramping operation does not affect it), one can finally derive (9) and (10), which refer to the lower and upper solid lines of the gray signal support, respectively . These are reported in the following for completeness without explicit derivation:

$$f_{min} = \begin{cases} -\frac{B_{\mathrm{TX}}}{2} + \left(t_{\mathrm{RRTT}} + \frac{T_{\mathrm{EWL}}}{2} + \frac{B_{\mathrm{img}}}{k_{\mathrm{r}}}\right) \cdot k_{\mathrm{r}}, \\ \quad \text{for } t_{\mathrm{RRTT}} < -\frac{T_{\mathrm{EWL}}}{2} - \frac{B_{\mathrm{img}}}{k_{\mathrm{r}}}, \\ t_{\mathrm{RRTT}} \cdot k_{\mathrm{FScan}} - \frac{1}{2}B_{\mathrm{img,FScan}}, \ \text{elsewhere,} \end{cases} \tag{A.10}$$

$$f_{max} = \begin{cases} \frac{B_{\mathrm{TX}}}{2} - \left(t_{\mathrm{RRTT}} - \frac{T_{\mathrm{EWL}}}{2} - \frac{B_{\mathrm{img}}}{k_{\mathrm{r}}}\right) \cdot k_{\mathrm{r}}, \\ \quad \text{for } t_{\mathrm{RRTT}} > \frac{T_{\mathrm{EWL}}}{2} + \frac{B_{\mathrm{img}}}{k_{\mathrm{r}}}, \\ t_{\mathrm{RRTT}} \cdot k_{\mathrm{FScan}} + \frac{1}{2}B_{\mathrm{img,FScan}}, \ \text{elsewhere.} \end{cases} \tag{A.11}$$

APPENDIX B
DISCUSSION ON TOPOGRAPHY DEPENDENCE

The analysis presented in Sections III and IV of the paper, in particular equations (9) and (10), assumes a linear dependency of the FScan frequency support on fast time/slant range. Strictly speaking, this will not be the case for a real system, where a linear relationship of scanning look angle and frequency is assumed. Here we present two numerical evaluations for quantifying the deviations. The chosen parameterization is for a mid swath look angle of 36° and fixed chirp lengths of 243 µs (used in the timing diagram) and 100 µs (used for the quantitative evaluation of data volume reduction) for the proposed BF-BAQ.

The diagrams in Figure A.2 on the left show the time-frequency support along with frequencies of the near (blue line), mid (green) and far (red) chirps. The dotted line indicates the linear approximation of the central scan frequency used in the paper. The black solid line assumes constant topography at the reference level, while the dotted one assumes a linear approximation. The dashed line shows the margins of the instantaneous bandwidth $B_{\mathrm{img,FScan}}$. Each chirp signal has a valid bandwidth of B_{img} of 300 MHz. The magenta line shows the central scan frequency for a topography mismatch of 1000 m. For the two cases, the linear approximation is accurate to about 15 MHz / 14 MHz (or +/-7.5 MHz / +/-7 MHz if balanced with near/far range), whereas the topography mismatch causes additional 40 MHz / 58 MHz. The following observations can be made:

- The echo window length is larger for shorter chirp length, as indicated in (3).
- The instantaneous bandwidth equals the deramped frequency range, $B_{\mathrm{img,FScan}}$, and is larger for larger chirp length, as indicated in (7).

The time-frequency support is $T_{\mathrm{ewl}} \cdot B_{\mathrm{TX}}$ and becomes smaller with increasing chirp length. In consequence, the data compression potential is larger for short chirp lengths. It can be quantified with respect to the fully overlapped FScan mode (with no data compression potential) as:

$$\mathrm{DVR}_{\mathrm{FScan}} = 1 - \frac{T_{\mathrm{ewl,full}}}{T_{\mathrm{ewl}}}. \tag{A.12}$$

This is the theoretical equivalent to the DVR in (15) and can easily be derived from (1) and (3). For the displayed cases in Figure A.2, DVR_{FScan} is 48% and 53.7%, respectively. For the BF-BAQ implementation of an operational system, two recommendations are given:

- Depending on the topography variation within the scene, a margin can be considered for the computation of the run length coding, i.e. f_{min} and f_{max} in (9) and (10) can be slightly decreased/increased.
- Instead of the linear approximation, one may compute the exact limits from the geometry, which may consider also the varying topography at a low resolution. However, this would require lots of additional computations when performed in an azimuth-adaptive way.

If none of the two choices are taken into consideration, the resulting data may suffer from a small degradation of SNR, whenever the quantized energy is not taken in a symmetric way around the central frequency line. The resolution and sidelobe levels will hardly be affected. However, for a given system, these effects should be investigated more in detail.

REFERENCES

[1] E. Rignot and J. van Zyl, "Change detection techniques for ERS-1 SAR data," *IEEE Transactions on Geoscience and Remote Sensing*, vol. 31, no. 4, pp. 896–906, 1993.

[2] G. Krieger, N. Gebert, and A. Moreira, "Unambiguous SAR signal reconstruction from nonuniform displaced phase center sampling," *IEEE Geoscience and Remote Sensing Letters*, vol. 1, no. 4, pp. 260–264, 2004.

[3] N. Yagüe-Martínez, P. Prats-Iraola, F. Rodríguez González, R. Brcic, R. Shau, D. Geudtner, M. Eineder, and R. Bamler, "Interferometric processing of Sentinel-1 TOPS data," *IEEE Transactions on Geoscience and Remote Sensing*, vol. 54, no. 4, pp. 2220–2234, 2016.

[4] C. Wecklich, M. Martone, P. Rizzoli, J.-L. Bueso-Bello, C. Gonzalez, and G. Krieger, "Production of a global forest/non-forest map utilizing TanDEM-X interferometric SAR data," in *2017 IEEE International Geoscience and Remote Sensing Symposium (IGARSS)*, 2017, pp. 751–754.

[5] A. Monti Guarnieri and C. Prati, "ScanSAR focusing and interferometry," *IEEE Transactions on Geoscience and Remote Sensing*, vol. 34, no. 4, pp. 1029–1038, 1996.

[6] F. De Zan and A. Monti Guarnieri, "TOPSAR: Terrain Observation by Progressive Scans," *IEEE Transactions on Geoscience and Remote Sensing*, vol. 44, no. 9, pp. 2352–2360, 2006.

[7] M. Bartusch, C. Bruens, A. E. Nuncio Quiroz, and S. Stettner, "HRWS: The upcoming german X-band spaceborne SAR mission," in *EUSAR 2021; 13th European Conference on Synthetic Aperture Radar*, 2021, pp. 1–4.

[8] M. Suess, B. Grafmueller, and R. Zahn, "A novel high resolution, wide swath SAR system," in *2001 IEEE International Geoscience and Remote Sensing Symposium (IGARSS)*, vol. 3, 2001, pp. 1013–1015 vol.3.

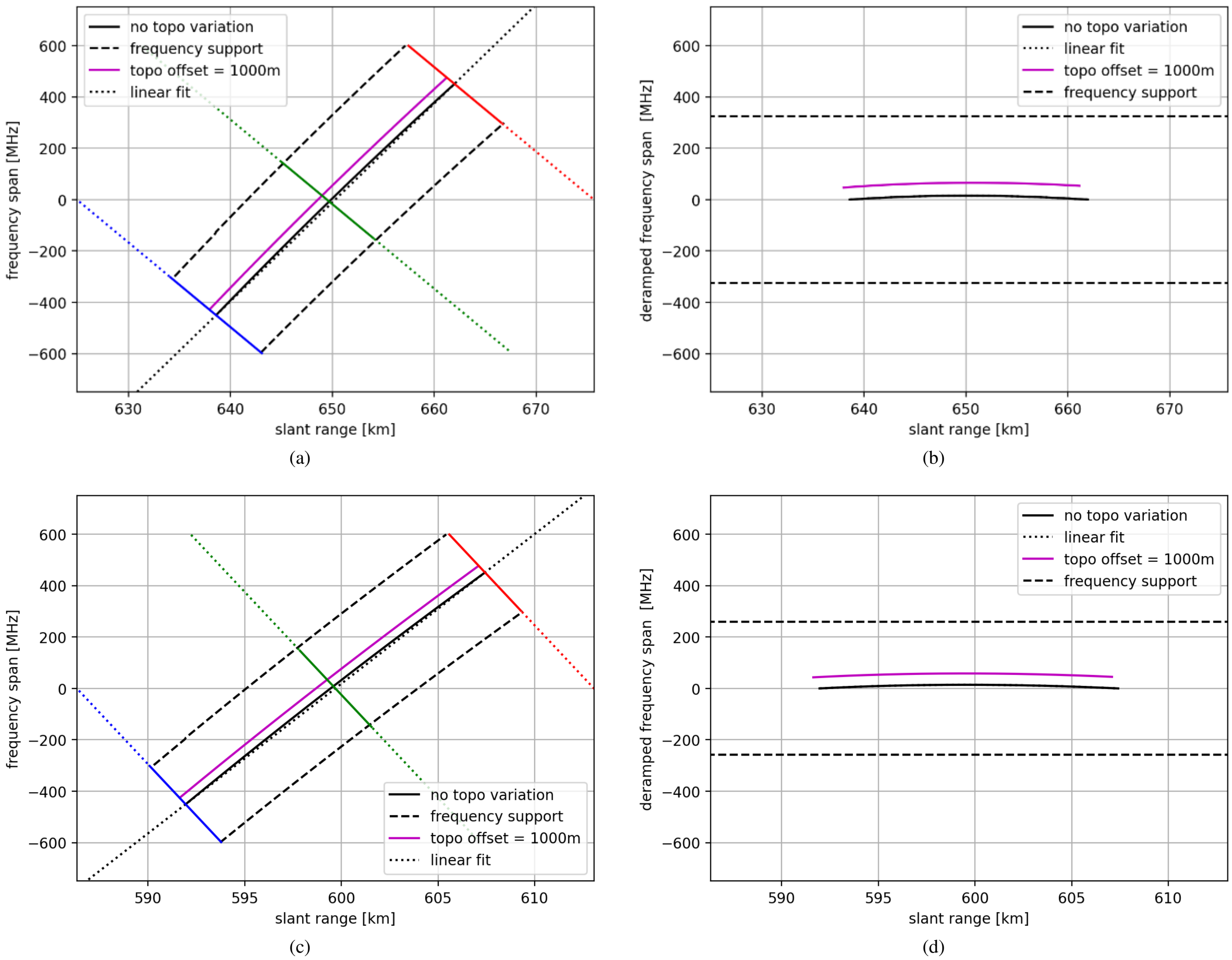

Fig. A.2: Time-frequency support for FScan mode for 80km swath width at mid swath 36° look angle: for the 243 µsec chirp length (top) and for a 50km swath and 100 µsec chirp length (bottom). The figures on the right show the center frequency line after deramping with linear approximation. The magenta lines describe the influence of topography.

[9] N. Gebert, G. Krieger, and A. Moreira, "Digital beamforming for HRWS-SAR imaging: System design, performance and optimization strategies," in *2006 IEEE International Symposium on Geoscience and Remote Sensing (IGARSS)*, 2006, pp. 1836–1839.

[10] F. Bordoni, M. Younis, and G. Krieger, "Performance investigation on the high-resolution wide-swath SAR system operating in multisubpulse mode," in *2012 IEEE International Geoscience and Remote Sensing Symposium*, July 2012, pp. 3568–3571.

[11] M. Villano, G. Krieger, and A. Moreira, "Staggered SAR: High-resolution wide-swath imaging by continuous PRI variation," *IEEE Transactions on Geoscience and Remote Sensing*, vol. 52, pp. 4462–4479, 2014.

[12] F. Q. de Almeida, M. Younis, G. Krieger, and A. Moreira, "A new slow PRI variation scheme for multichannel SAR high-resolution wide-swath imaging," in *2018 IEEE International Geoscience and Remote Sensing Symposium (IGARSS)*, 2018, pp. 3655–3658.

[13] F. Bordoni, M. Younis, and G. Krieger, "Synthetik-aperturradarverfahren," https://depatisnet.dpma.de/, Jun. 26 2014, german Patent Application DE102013216461A1, [online].

[14] F. Bordoni, G. Krieger, and M. Younis, "Multifrequency subpulse SAR: Exploiting chirp bandwidth for an increased coverage," *IEEE Geoscience and Remote Sensing Letters*, vol. 16, pp. 40–44, 2019.

[15] C. Roemer, "Introduction to a new wide area SAR mode using the F-SCAN principle," in *2017 IEEE International Geoscience and Remote Sensing Symposium (IGARSS)*, 2017, pp. 3844–3847.

[16] L. Nan, G. Gai, T. Shiyang, and Z. Linrang, "Signal modeling and analysis for elevation frequency scanning HRWS SAR," *IEEE Transactions on Geoscience and Remote Sensing*, vol. 58, no. 9, pp. 6434–6450, 2020.

[17] D. C. Lancashire, B. A. Barnes, and S. J. Udall, "Block adaptive quantization," Jul. 3 2001, US Patent 6,255,987.

[18] R. Kwok and W. Johnson, "Block adaptive quantization of magellan sar data," *IEEE Transactions on Geoscience and Remote Sensing*, vol. 27, no. 4, pp. 375–383, 1989.

[19] P. Snoeij, E. Attema, A. M. Guarnieri, and F. Rocca, "FDBAQ a novel encoding scheme for Sentinel-1," in *2009 IEEE International Geoscience and Remote Sensing Symposium (IGARSS)*, vol. 1, 2009, pp. I–44–I–47.

[20] P. Guccione, M. Belotti, D. Giudici, A. Monti Guarnieri, and I. Navas-Traver, "Sentinel-1A: Analysis of FDBAQ performance on real data," *IEEE Transactions on Geoscience and Remote Sensing*, vol. 53, no. 12, pp. 6804–6812, 2015.

[21] M. Martone, M. Villano, M. Younis, and G. Krieger, "Efficient onboard quantization for multichannel SAR systems," *IEEE Geoscience and Remote Sensing Letters*, vol. 16, no. 12, pp. 1859–1863, 2019.

[22] M. Martone, N. Gollin, M. Villano, P. Rizzoli, and G. Krieger, "Predictive quantization for data volume reduction in staggered SAR systems," *IEEE Transactions on Geoscience and Remote Sensing*, vol. 58, pp. 5575–5587, 2020.

[23] R. Scheiber, M. Martone, and N. Gollin, "Chirp selection and data compression for spaceborne wide-swath SAR in FScan-mode," in *EUSAR*

2021; 13th European Conference on Synthetic Aperture Radar, 2021, pp. 1–6.

[24] G. Krieger, N. Gebert, and A. Moreira, "Multidimensional waveform encoding: A new digital beamforming technique for synthetic aperture radar remote sensing," *IEEE Transactions on Geoscience and Remote Sensing*, vol. 46, no. 1, pp. 31–46, 2008.

[25] G. Krieger, A. Moreira, H. Fiedler, I. Hajnsek, M. Werner, M. Younis, and M. Zink, "TanDEM-X: A Satellite Formation for High-Resolution SAR Interferometry," *IEEE Transactions on Geoscience and Remote Sensing*, vol. 45, no. 11, pp. 3317–3341, 2007.

[26] M. Zink, A. Moreira, I. Hajnsek, P. Rizzoli, M. Bachmann, R. Kahle, T. Fritz, M. Huber, G. Krieger, M. Lachaise, M. Martone, E. Maurer, and B. Wessel, "TanDEM-X: 10 years of formation flying bistatic SAR interferometry," *IEEE Journal of Selected Topics in Applied Earth Observations and Remote Sensing*, vol. 14, pp. 3546–3565, Feb 2021.

[27] P. Guccione, M. Scagliola, and D. Giudici, "Principal components dynamic block quantization for multichannel SAR," in *2016 IEEE International Geoscience and Remote Sensing Symposium (IGARSS)*, 2016, pp. 2090–2093.

[28] J. Mittermayer, M. Younis, R. Metzig, S. Wollstadt, J. Marquez Martinez, and A. Meta, "Terrasar-x system performance characterization and verification," *IEEE Transactions on Geoscience and Remote Sensing*, vol. 48, no. 2, pp. 660–676, 2010.

[29] J. Fischer, U. Benz, and A. Moreira, "Efficient SAR raw data compression in frequency domain," in *1999 IEEE International Geoscience and Remote Sensing Symposium (IGARSS)*, vol. 4, 1999, pp. 2261–2263 vol.4.

[30] U. Benz, K. Strodl, and A. Moreira, "A comparison of several algorithms for SAR raw data compression," *IEEE Transactions on Geoscience and Remote Sensing*, vol. 33, no. 5, pp. 1266–1276, 1995.

[31] M. Martone, N. Gollin, P. Rizzoli, and G. Krieger, "Performance-optimized quantization for SAR and InSAR applications," *IEEE Transactions on Geoscience and Remote Sensing*, 14 Jun. 2022.

[32] R. Lyons, "Digital signal processing," *New York*, pp. 23–54, 2006.

[33] T. Kraus, D. Schrank, P. Rizzoli, and B. Bräutigam, "In-orbit SAR performance of TerraSAR-X and TanDEM-X satellites," in *Proceedings of URSI Commission F-Triennial Open Symposium on Radio Wave Propagation and Remote Sensing*, 2011, pp. 1–6.

[34] S. Hensley, S. Smrekar, S. Shaffer, M. Paller, H. Figueroa, A. Freeman, R. Hodges, and P. Walkemeyer, "VISAR: A next generation interferometric radar for venus exploration," in *2015 IEEE 5th Asia-Pacific Conference on Synthetic Aperture Radar (APSAR)*, 2015, pp. 362–366.

[35] S. Huber and G. Krieger, "The TanDEM-X mission: Overview and interferometric performance," in *2009 European Radar Conference (EuRAD)*, 2009, pp. 25–28.

[36] M. Martone, B. Bräutigam, and G. Krieger, "Quantization effects in TanDEM-X data," *IEEE Transactions on Geoscience and Remote Sensing*, vol. 53, no. 2, pp. 583–597, 2015.

[37] I. G. Cumming and F. H. Wong, "Digital processing of synthetic aperture radar data," *Artech house*, vol. 1, no. 3, pp. 111–231, 2005.

[38] R. Clarke, *Transform coding of images*. Academic Press Professional, Inc., 1985.

[39] V. Goyal, "Theoretical foundations of transform coding," *IEEE Signal Processing Magazine*, vol. 18, no. 5, pp. 9–21, 2001.

[40] M. Martone, B. Bräutigam, and G. Krieger, "Azimuth-switched quantization for SAR systems and performance analysis on TanDEM-X data," *IEEE Geoscience and Remote Sensing Letters*, vol. 11, no. 1, pp. 181–185, 2014.

Nicola Gollin received the M.Sc. degree in information and communication engineering from the Università degli Studi di Trento, Trento, Italy, in 2018, with a thesis on predictive quantization for data volume reduction in staggered synthetic aperture radar (SAR) systems, pursued at the Microwaves and Radar Institute, German Aerospace Center (DLR), Wessling, Germany. Since 2018, he has been with the System Performance Group, Microwaves and Radar Institute, German Aerospace Center (DLR), where he is currently a Project Engineer. His research interests include signal processing applied to synthetic aperture radar, and the analysis and design of future SAR systems. Mr. Gollin received the Best Paper Award at the German Microwave Conference and the ARGUS Science Award, both in 2019.

Rolf Scheiber Rolf Scheiber received the Dipl.-Ing. (M.S.) degree in electrical engineering from the Technical University of Munich, Germany in 1994 and the Dr.-Ing. (PhD) degree in 2003 also in electrical engineering from the University of Karlsruhe, Germany with a thesis on airborne SAR interferometry. Since 1994 he has been with the German Aerospace Center (DLR), Microwaves and Radar Institute, where he developed the first operational high precision interferometric SAR processor for its E-SAR airborne sensor. Since 2001 he is heading the Signal Processing Group within the SAR Technology Department, where he is supervising the DLR's F-SAR and DBFSAR airborne SAR processing activities. Dr. Scheiber supported several demonstrator projects for spaceborne SAR, among which the first demonstration of the new TOPS imaging mode of Sentinel-1 with TerraSAR-X data and the development of the staring spotlight mode SAR procesor for TerraSAR-X. He has authored or co-authored 40 peer-reviewed journal papers, more than 200 conference papers and holds 3 patents. His research interests include algorithm development for air- and spaceborne SAR focussing, motion compensation, SAR interferometry, DEM generation, differential SAR interferometry, SAR tomography, circular SAR as well as radio ice-sounding algorithms and applications.

Michele Martone received the B.Sc. and M.Sc. degrees in telecommunication engineering from the University of Naples Federico II, Naples, Italy, in 2006 and 2009, respectively, and the Ph.D. degree from the Karlsruhe Institute of Technology, Karlsruhe, Germany, in 2019. Since 2009, he has been with the German Aerospace Center (DLR), Microwaves and Radar Institute, Wessling, Germany, where he has participated in the development and optimization of the TerraSAR-X and TanDEM-X spaceborne SAR missions, the generation of the global TanDEM-X digital elevation model and Forest/Non-Forest map, and has been involved in several projects in collaboration with research and industry partners focused on the design of future SAR missions. He has authored or coauthored nearly 100 research articles in peer-reviewed journals and international conference proceedings and holds two patents in the field of SAR. His research interests include the design of innovative SAR systems with particular focus on the development of efficient quantization and data volume reduction methods. Dr. Martone has been a member of technical program committee for several international conferences and workshops and is member of the Consultative Committee for Space Data Systems (CCSDS). He was the recipient of the DLR Science Award in 2018 and of the Best Paper Award at the German Microwave Conference 2019, and regularly serves as a reviewer for the IEEE TRANSACTIONS ON GEOSCIENCE AND REMOTE SENSING, the IEEE GEOSCIENCE AND REMOTE SENSING LETTERS and the IEEE JOURNAL OF SELECTED TOPICS IN APPLIED EARTH OBSERVATIONS AND REMOTE SENSING.

Paola Rizzoli received the B.Sc. (2003) and M.Sc. (2006) degrees in telecommunication engineering from the Politecnico di Milano University (Polimi), Milan, Italy, and the Ph.D. degree (2018, summa cum laude) in electrical engineering and information technology from the Karlsruhe Institute of Technology (KIT), Karlsruhe, Germany. From 2006 to 2008, she was with the Politecnico di Milano and Aresys s.r.l., a Polimi spin-off company, as Scientific Researcher and Project Engineer. At the end of 2008, she joined the Microwaves and Radar Institute at the German Aerospace Center (DLR), Oberpfaffenhofen, Germany, as Project Engineer, where she has been involved in the development and optimization of the TerraSAR-X and TanDEM-X missions, concentrating, in particular, on the generation of the TanDEM-X global digital elevation model. From 2016 to 2020, she led the System Performance Research Group of the Satellite SAR Systems Department, being responsible for the final performance assessment of the global TanDEM-X DEM and the generation of the global TanDEM-X Forest/Non-Forest map. Since 2020 she has been leading the Radar Science Research Group. Her main research interests include SAR systems design, data reduction techniques, estimation theory, signal processing, and artificial intelligence algorithms. Dr. Rizzoli received the DLR Science Award in 2018 and the Best Paper Award at the German Microwave Conference in 2019. She regularly serves as a reviewer for the IEEE TRANSACTIONS ON GEOSCIENCE AND REMOTE SENSING, the IEEE GEOSCIENCE AND REMOTE SENSING LETTERS and the IEEE JOURNAL OF SELECTED TOPICS IN APPLIED EARTH OBSERVATIONS AND REMOTE SENSING.

Gerhard Krieger (M'04-SM'09-F'13) received the Dipl.-Ing. (M.S.) and Dr.-Ing. (Ph.D.) (Hons.) degrees in electrical and communication engineering from the Technical University of Munich, Germany, in 1992 and 1999, respectively. From 1992 to 1999, he was with the Ludwig Maximilians University, Munich, where he conducted multidisciplinary research on neuronal modeling and nonlinear information processing in biological and technical vision systems. Since 1999, he has been with the Microwaves and Radar Institute of the German Aerospace Center (DLR), Oberpfaffenhofen, Germany, where he started as a research associate developing signal processing algorithms for a novel forward-looking radar system employing digital beamforming on receive. From 2001 to 2007, he led the New SAR Missions Group which pioneered the development of advanced bistatic and multistatic radar systems, such as TanDEM-X, as well as innovative multichannel SAR techniques and algorithms for high-resolution wide-swath SAR imaging. Since 2008, he has been the Head of the Radar Concepts Department which hosts about 40 scientists focusing on new SAR techniques, missions and applications. He has been serving as Mission Engineer for TanDEM-X and he made also major contributions to the development of the Tandem-L mission concept, where he led the Phase-0 and Phase-A studies. Since 2019, he holds also professorship at the Friedrich-Alexander-University Erlangen, Germany. Gerhard Krieger is author or co-author of more than 100 peer-reviewed journal papers, 9 invited book chapters, more than 400 conference papers, and more than 20 patents. Prof. Krieger has been an Associate Editor for the IEEE Transactions on Geoscience and Remote Sensing since 2012. In 2014, he served as the Technical Program Chair for the European Conference on Synthetic Aperture Radar and as a Guest Editor for the IEEE Journal of Selected Topics in Applied Earth Observations and Remote Sensing. He received several national and international awards, including two Best Paper Awards at the European Conference on Synthetic Aperture Radar, two Transactions Prize Paper Awards of the IEEE Geoscience and Remote Sensing Society, and the W.R.G. Baker Prize Paper Award from the IEEE Board of Directors.